Article

Cell Systems

Design and Analysis of a Proportional-Integral-Derivative Controller with Biological Molecules

Graphical Abstract

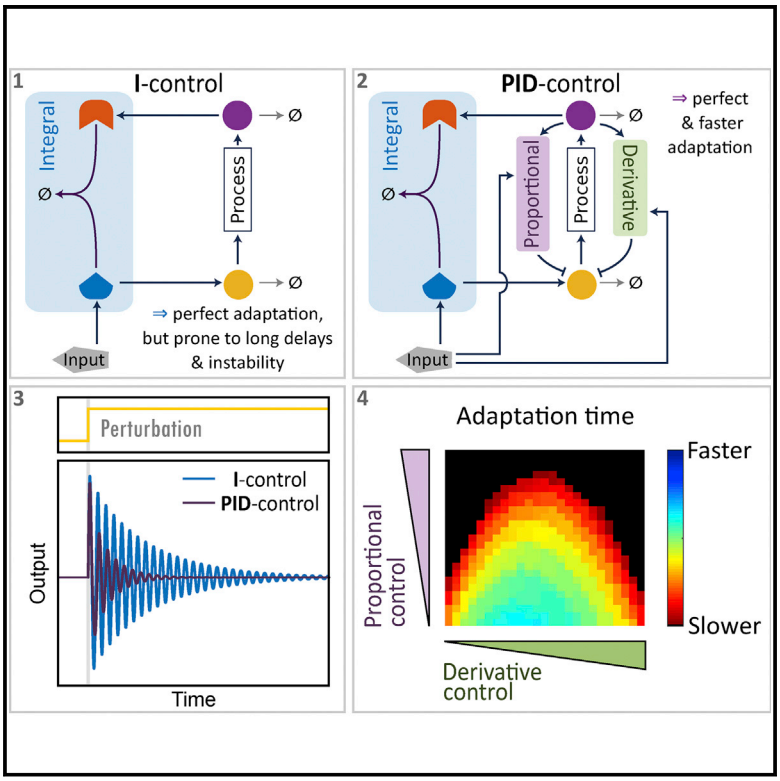

Highlights

- Integral control allows perfect adaptation but can be slow or even unstable
- Molecular proportional and derivative control modules improve adaptation performance
- Control modules can be composed in a modular fashion to achieve design specifications

Authors

Michael Chevalier, Mariana Gómez-Schiavon, Andrew H. Ng, Hana El-Samad

Correspondence

michael.chevalier@ucsf.edu (M.C.), hana.el-samad@ucsf.edu (H.E.-S.)

In Brief

Antithetic feedback is a general method for integral (I) control in biological systems. We present design and analysis of biomolecular equivalents of proportional (P) and derivative (D) control. Together, P, I, and D modules can be combined to generate PID control or any variation thereof for the control of biological systems within desired dynamic specifications.

Chevalier et al., 2019, Cell Systems 9, 1–16
October 23, 2019
https://doi.org/10.1016/j.cels.2019.08.010

CellPress

Please cite this article in press as: Chevalier et al., Design and Analysis of a Proportional-Integral-Derivative Controller with Biological Molecules, Cell Systems (2019), https://doi.org/10.1016/j.cels.2019.08.010

Cell Systems
Article

Design and Analysis of a Proportional-Integral-Derivative Controller with Biological Molecules

Michael Chevalier,[1,4,5,*] Mariana Gómez-Schiavon,[1,4] Andrew H. Ng,[2] and Hana El-Samad[1,2,3,*]
[1]Department of Biochemistry and Biophysics, University of California, San Francisco, 600 16th St., San Francisco, CA 94158, USA
[2]Cell Design Initiative, University of California, San Francisco, San Francisco, CA 94150, USA
[3]Chan-Zuckerberg Biohub, 499 Illinois St., San Francisco, CA 94158, USA
[4]These authors contributed equally
[5]Lead Contact
*Correspondence: michael.chevalier@ucsf.edu (M.C.), hana.el-samad@ucsf.edu (H.E.-S.)
https://doi.org/10.1016/j.cels.2019.08.010

SUMMARY

The capability to engineer *de novo* feedback control with biological molecules is ushering in an era of robust functionality for many applications in biotechnology and medicine. To fulfill their potential, these control strategies need to be generalizable, modular, and operationally predictable. Proportional-integral-derivative (PID) control fulfills this role for technological systems. Integral feedback control allows a system to return to an invariant steady-state value after step disturbances. Proportional and derivative feedback control used with integral control modulate the dynamics of the return to steady state following perturbation. Recently, a biomolecular implementation of integral control was proposed based on an antithetic motif in which two molecules interact stoichiometrically to annihilate each other's function. In this work, we report how proportional and derivative implementations can be layered on top of this integral architecture to achieve a biochemical PID control design. We investigate computationally and analytically their properties and ability to improve performance.

INTRODUCTION

In both biology and engineering, integral feedback control can ensure perfect adaptation, that is, the ability to return to a desired set point after a perturbation. Because of its widespread successful use in engineering, and its natural occurrence in biology, modular and robust implementations of integral control have been actively pursued in synthetic biology. A breakthrough design of an integral control scheme based on a simple "antithetic motif" was recently reported (Briat et al., 2016). In this design, two molecular species bind to each other and annihilate each other's function through this binding (Figure 1A). If one of the "antithetic" molecular species controls the input of a process Φ while the other is dependent on the output of Φ, then it can be mathematically demonstrated that the steady-state value of the output of Φ perfectly adapts regardless of any step perturbation that Φ is subjected to. The antithetic motif used in this configuration, therefore, implements integral feedback action necessary to achieve perfect adaptation. An initial experimental proof of concept based on the antithetic feedback motif was recently tested in *E. coli* using σ and anti-σ factors to implement the antithetic reaction, and the results suggest that this feedback method is indeed able to implement integral control *in vivo* (Aoki et al., 2019).

Integral control has limitations; it can be prone to problems such as long delays and oscillations before returning to the steady state (due to poor damping) or inability to return to the steady state (due to limit cycles), and this has been shown to occur for the antithetic motif as well (Briat et al., 2016). To overcome these limitations, traditionally, integral control is used in combination with other control strategies, such as proportional and derivative control (Figure 1B). Proportional (P) control uses the instantaneous regulation error between the desired set point and the output of the process Φ to be controlled and by doing so, it can increase the speed of response. Derivative (D) control uses the time derivative of the regulation error signal. It can reduce overshoot and increase the convergence rate to steady state. Finally, integral (I) control uses the integral of the error signal. Signals from P, I, and D are summed to generate the control signal $u(t)$—that is, the signal that is generated by the combined PID controller and is then inputted to the process Φ in order to control it (Figure 1B) (Bennett, 1993). For many applications in engineering, this combination has been shown to provide more robust performance than any control term alone.

Our aim is to improve upon the antithetic integral control motif in much the same way PID control improves on integral control. Although other strategies exist to implement adaptation in the biological context (Alon et al., 1998; Yi et al., 2000; El-Samad et al., 2002; Muzzey et al., 2009), including incoherent feedforward loops, which are prevalent in nature (Mangan et al., 2006), we have chosen to focus on proportional and derivative control in this work. We ask how P and D control can be designed to enable implementation of PI, ID, or PID biomolecular control schemes in cells. As discussed in Box 1, we have chosen to take a theoretical approach to this problem because we believe that theory plays a useful role in guiding future experiments that may be presently impractical. However, we caution that because the biological context is idiosyncratic, we cannot be certain that P, I, and D control will be as easy to implement and tune in biology or combine in

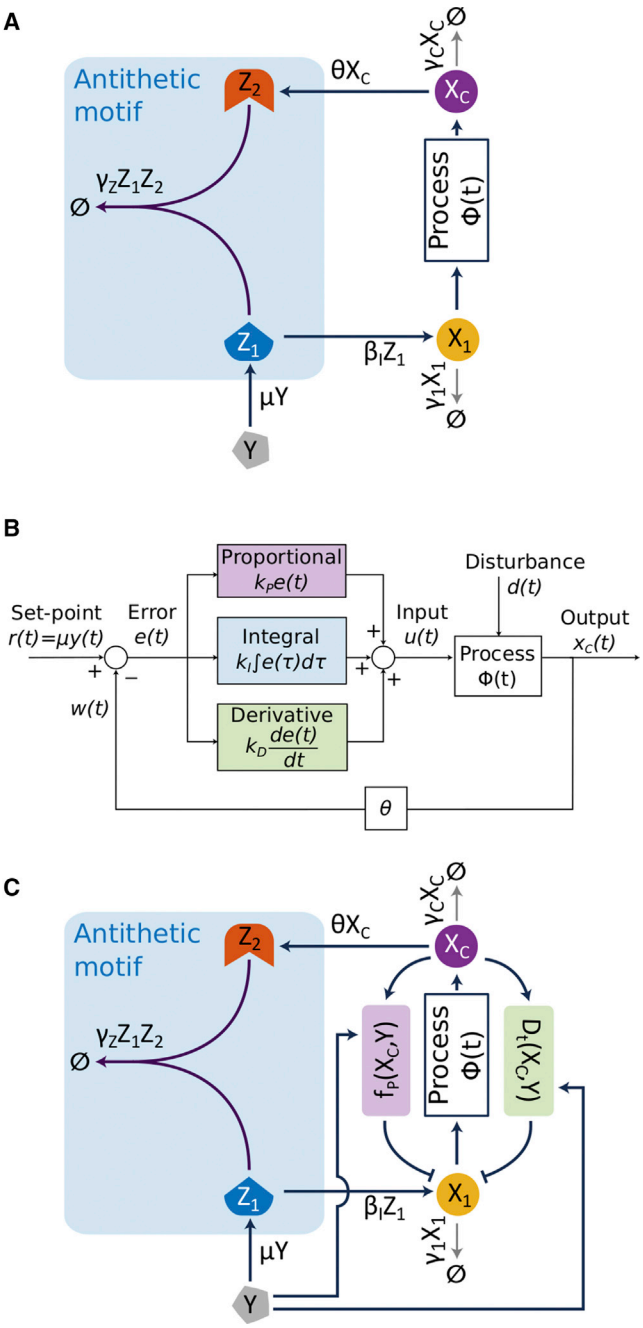

Figure 1. Schematics of an Engineering and Biomolecular Proportional-Integral-Derivative Controller

(A) Schematic of biomolecular integral (I) control using the antithetic motif (blue box) circuit from Briat et al. (2016). The integral control term ($\beta_I Z_1$) actuates X_1, which is the first molecular species of the controlled process $\Phi(t)$.

(B) Traditional textbook schematic of PID control: time-dependent regulation error, $e(t) = r(t) - w(t) = \mu y(t) - \theta x_C(t)$, is continuously computed and processed by the proportional, integral, and derivative control terms. The control terms are summed up to generate $u(t)$, the control action that is then fed into the process $\Phi(t)$. The objective is to eliminate the regulation error signal $e(t)$, driving it to zero after a disturbance to the process.

(C) Schematic of biomolecular PID control. This design builds on the antithetic motif (blue box). We add proportional (purple box) and derivative (green box) modules. Like in the traditional PID design, the integral control term ($\beta_I Z_1$), the proportional control term ($f_P(X_C,Y)$) and derivative control term ($D_t(X_C,Y)$) are additive in the actuation of X_1, which is the first molecular species of the controlled process $\Phi(t)$.

practice as they have been in more traditional engineering contexts.

In this paper, we present the design of a biomolecular PID control system, based on the antithetic integral (I) control motif (Figure 1C). Our design of proportional (P) control proceeds through the development of a nonlinear function that implicitly contains a scaled subtraction of the set point and process output (that is, the regulation error). For the derivative (D) control design, we draw inspiration from the *E. coli* chemotaxis regulatory network (Barkai and Leibler, 1997), which is capable of measuring the time-dependent changes in chemoattractant concentrations, naturally implementing an approximate derivative motif. We demonstrate, through analytical treatments and numerical simulations, how the addition of proportional and derivative control to integral control improves transient adaptation dynamics. We further show how our designs relate to a traditional engineering PID controller and illustrate how such analogy facilitates the choice of parameters for the P, I, and D control functions as well as their effective weights (k_I , k_P , k_D). Finally, we discuss how the modularity of the proposed PID control allows substitution of different integral controllers, demonstrating that the P and D control terms are compatible with different forms of integral control. Our theoretical work paves the way for experimental studies aimed at modular, general, and robust implementation of PID control with biological parts.

RESULTS

In a landmark paper by Briat et al. (2016), a simple integral scheme was proposed to control a general biological process Φ. If the output of the process is X_C and its input (that is actuated by the control signal) is X_1 (Figure 1A), then this scheme in the deterministic regime is given by:

$$\frac{dZ_1}{dt} = \mu Y - \eta Z_1 Z_2 \qquad \text{(Equation 1)}$$

$$\frac{dZ_2}{dt} = \theta X_C - \eta Z_1 Z_2 \qquad \text{(Equation 2)}$$

$$\frac{dX_1}{dt} = \beta_I Z_1 - \gamma_1 X_1 \qquad \text{(Equation 3)}$$

Equations 1 and 2 were produced by an antithetic motif in which two molecules Z_1 and Z_2 bind and annihilate each other's activity with mass-action kinetics. Z_1 is produced at some rate μY and influences the production of the process-actuated molecule X_1 in Equation 3. Z_2 is produced at a rate θX_C, proportional to the output of the process Φ, hence closing the loop (Figure 1A, anthithetic module in blue). The equation describing $Z = Z_1 - Z_2$ is given by:

$$\frac{dZ}{dt} = \frac{dZ_1}{dt} - \frac{dZ_2}{dt} = \mu Y - \theta X_C \qquad \text{(Equation 4)}$$

Box 1. Control Theory in Biology—a Philosophical Discussion

A foundational question of cell engineering, as it matures, is whether it should proceed like it has in the past—by adopting mimicry of designs commonly found in technological circuits—or whether it should invent new designs that are best tailored to the biological substrate. We are of the philosophy that the most practical way to explore the latter option is through developing theory that is agnostic when it comes to precise biochemical or biological implementation.

There are several reasons we hold this philosophy. Here, we discuss one and its implications. One might argue that while our knowledge of biological macromolecules may approach the comprehensive, we still have very little understanding of what the **unit of selectable biological function** is in any particular biological context. The consequences of this lack of knowledge are far from trivial. The majority of synthetic biology to date has proceeded by seeking to design a function, examining its implementation in engineering of technological systems, and then identifying biological "parts" that if composed in prescribed ways, can approximate the technological implementation. If such biological "parts" do not have a clear definition, being instead (for example) probabilistic associations of redundant groups of molecules that require a particular context or history for function, then it might be the case that we are yet to understand the design space of biology even for the simplest functions. However, by using theory, we can begin to understand mathematically how these "parts" must work together, even if they remain undefined. It is exciting to imagine that the upgrade to integral, proportional or derivative control, for example, might take forms that we are yet to invent, or maybe that the notion itself of these types of control will be in need of a more adequate biological replacement.

This raises the question of whether theory should outpace its practice. This is a question that other fields of engineering have encountered before. For example, before digital computers, even integral control was an elaborate undertaking with non-trivial constraints on realization. However, theory established that integral feedback, when used on a linear dynamical system, can robustly steer a regulated system variable to a desired set point, while achieving perfect adaptation to disturbances, regardless of the model parameters (Francis and Wonham, 1976). Importantly, this seminal theoretical paper did not prescribe any particular implementation with mechanical or electronic components. Similarly, in biology, zero-order ultrasensitivity—a sharp, thresholded output response of a signaling network that occurs when signaling proteins are operating near saturation—was a theoretical construct at first. The theory of cooperativity to explain thresholded dose responses was largely driven by the attempt to explain the experimental sigmoidal oxygen-binding curve of hemoglobin. However, the theoretical postulation of zero-order ultrasensitivity as another implementation that can facilitate sigmoidal functions was not in response to any experimental data, nor to solve a biological mystery (Goldbeter and Koshland, 1981). The theory came first. Experimental discovery and different components and implementations followed. Therefore, we take inspiration from these examples where theory and practice have formed a powerful synergy, and argue that while implementation details should be a cornerstone of synthetic biology, the theory of what is possible, even if not immediately implementable, should be another.

This is especially true as different biological contexts may require the same general function to be performed to different levels of accuracy, precision, speed, robustness, etc. For example, the engineering of patient-derived T cells to treat cancers (Lim and June, 2017) has a completely different set of **design constraints** than a conceptually similar strategy for engineering a microorganism to produce value chemicals in batch culture (Chae et al., 2017; Dahl et al., 2013). We are of the philosophy that the design of a biological controller, like the design of any other system, should start with a list of the design goals and design constraints. The design goals could be considerations such as zero steady-state error (or full adaptation) after disturbance, fast response, little overshoot following inputs, or tracking an input with fidelity. Design constraints could be limitations that relate to the system to be controlled (e.g., its controllability and observability), the failure modes of the controller itself (e.g., integrator windup or amplification of noise) or related to implementing the controller itself such as its cost and feasibility or availability and precision of components. Controller design is almost always an acceptable compromise between these two lists. The complexity of design is also invariably linked to both goals and constraints. Simply stated, ideally, the number of design parameters in a controller should match the number of goals in the design, but these parameters are also influenced by the constraints—an engineering tug of war experienced by every engineer. In essence, our theoretical treatment of PID control in the paper aims to inform the choice between P, PI, PD and PID controllers at this level.

At steady state, $\frac{dZ}{dt} = 0 \Leftrightarrow \mu Y = \theta X_C$. Therefore, the steady-state output is given by $X_{C_{ss}} = \mu Y/\theta$, which is obviously independent of the process Φ and hence is achieved irrespective of Φ and despite any perturbation to its parameters. This is referred to as set-point tracking, since the output at steady state tracks the input Y. Equation 4 also implies that if the system is at steady state and a step change in the parameter values of Φ occurs, then X_C will return to its pre-perturbed value after an initial transient. This is the essence of the integral control action. One notes here that Z is only a mathematical regulation error quantity and not a physical quantity, as the production of X_1 involves Z_1 and not $Z_1 - Z_2$. Furthermore, the integral effect is contingent on two general requirements. First, the output X_C must be controllable in a positive manner by the actuated variable X_1 through the process Φ in order to preserve the corrective nature of the feedback through the antithetic motif. For example, saturation should not occur in the observed range of X_1, otherwise X_C cannot be effectively controlled. Second, the disappearance of Z_1 and Z_2 (either through degradation or inactivation) should only be achieved through their mutual annihilation, but not through any other process that affects one but not the other (such as individual degradation of Z_1 and Z_2).

While integral control achieves step disturbance rejection, it is seldom used alone in engineering applications. This is because

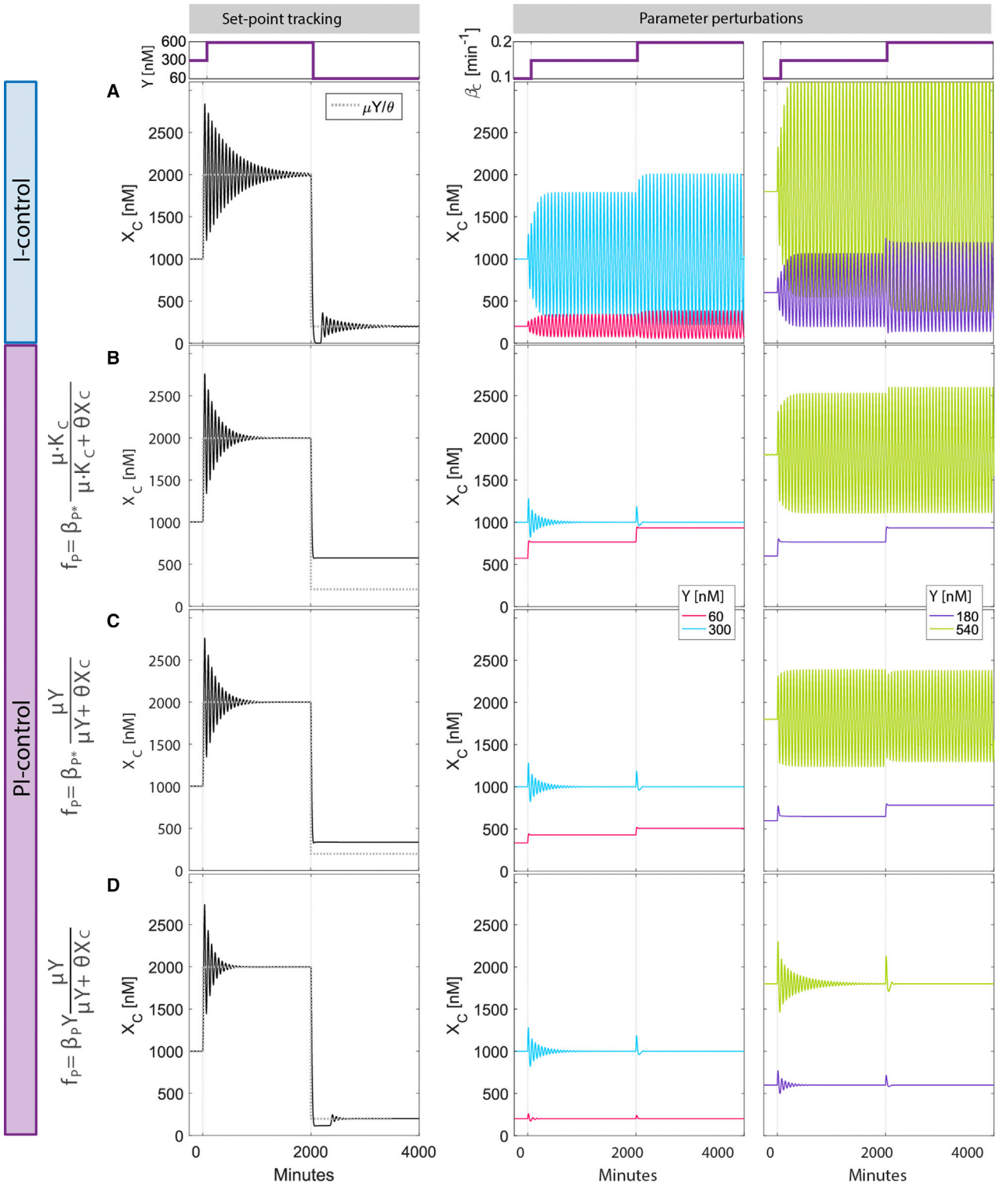

Figure 2. Proportional-Integral Control Can Produce Better Transient Dynamics than Integral Control Alone

(A) Time dynamics of output $X_C(t)$ following a change in the set-point Y (left panel) or in process parameter β_C (right panel). The outcome of β_C perturbation is also shown for different values of $Y = [60, 180, 300, 540]$ nM. Simulations are shown for process in Equation 5 and controller in Equations 6, 7, and 8 of main text. For I control, $f_P(X_C,Y) = 0$ and $D_t(X_C,Y) = 0$ in these equations.

(legend continued on next page)

integral control responds relatively slowly to disturbance, allowing for a large transient deviation from the desired steady state. This can lead to system instability and oscillations. To illustrate this point, we explore the same simple controlled process Φ described in Briat et al. (2016) in which X_1 is related to X_C through a gain β_C:

$$\frac{dX_C}{dt} = \beta_C X_1 - \gamma_C X_C, \qquad \text{(Equation 5)}$$

In this system, while perfect disturbance rejection is achieved for some parameter regimes, oscillations also easily emerged with Equations 1, 2, and 3 (which we refer to as I control) for the controlled process in Equation 5. This is shown in the left panel of Figure 2A that demonstrates how perfect tracking of the set point with I control is only achieved after a long period of damped oscillations. The right panel of Figure 2A shows the I control system undergoing sustained oscillations following a perturbation in β_C, a parameter of the controlled process. Because of this behavior, a commonly used modality in engineering combines integral control with proportional and derivative control, generating proportional-integral-derivative (PID) control. We therefore, aim to propose and analyze biochemical implementations of proportional and derivative control that augment and refine the integral control capabilities of the antithetic motif (Briat et al., 2016). To achieve this, we propose the following set of equations:

$$\frac{dZ_1}{dt} = \mu Y - \eta Z_1 Z_2 \qquad \text{(Equation 6)}$$

$$\frac{dZ_2}{dt} = \theta X_C - \eta Z_1 Z_2 \qquad \text{(Equation 7)}$$

$$\frac{dX_1}{dt} = \beta_I Z_1 + f_P(X_C, Y) + D_t(X_C, Y) - \gamma_1 X_1 \qquad \text{(Equation 8)}$$

The design upgrades actuation of X_1 with two additional terms, f_P (X_C,Y) for proportional control and D_t (X_C,Y) for derivative control (Figure 1C). In the designs we present below, f_P (X_C,Y) will be a function while D_t (X_C,Y) will be the output of a dynamical system with inputs X_C and Y. In the same way that the proportional, integral, and derivative control terms are summed up in the engineering PID diagram (Figure 1B), they are summed up in the equation for X_1. We propose an experimental implementation of this equation in STAR Methods "Experimental realization of X_1 equation." We next present designs and analyses that define these terms and their implementation with biomolecules.

Design of a Proportional Control Term

A traditional implementation of proportional control in the engineering sense would require an explicit computation of the tracking error, given by $e(t) = \mu Y - \theta X_C(t)$ in the context of Figure 1C. Since the outcome of any operation implemented with biological molecules is another molecule, computation of an error signal with biomolecules of this type can only generate a positive quantity. Following the example of the I control scheme, we will therefore design a proportional control function that acts implicitly on this error, without explicitly computing it.

The first consideration in the design is that for negative feedback (X_C is a negative regulator in the tracking error), the proportional control term f_P (X_C,Y) must be an inhibitory function of X_C. One option is to use a traditional Michaelis-Menten inhibitory function, $f_P(X_C, Y) = \beta_P \frac{\mu K_C}{\mu K_C + \theta X_C}$, which captures transcriptional repression of X_1 by X_C. Here, β_P represents the maximum synthesis rate in the absence of the inhibitor X_C, and μK_C is a constant related to the affinity or strength of the inhibitor (smaller K_C results in stronger inhibition for the same concentration of X_C). We include μ and θ in the representation of this function in order to keep the consistency of notation as it relates to the antithetic feedback description (Figures 1A and 1C). This type of transcriptional inhibition function has been explored in natural occurrences of cellular feedback, and previously used in synthetic biology applications (Purcell et al., 2010; Dahl et al., 2013), including adding proportional regulation to integral control (Briat et al., 2018). However, this function does not explicitly depend on Y unlike the tracking error $e(t)$. This disengagement between the set point and proportional term limits the dynamic range in a PI control system ($D_t(X_C, Y) = 0$ in Equations 6, 7, and 8). Specifically, at low reference set-point Y values (including $Y = 0$), both perfect tracking behavior and perfect adaptation following a change in β_C are lost (Figure 2B). This is because in this regime, the proportional term introduces basal synthesis of X_1, creating a basal level of X_C and hence of Z_2. At the same time, μY is too low so that insufficient Z_1 is produced to successfully overcome the basal Z_2 level. In fact, Z_2 grows at a positive constant rate since Z_1 is too low to contribute to its annihilation (see Figure S1A). The outcome is that the system is effectively operating in open loop, and the integral control is not satisfactorily active as evidenced by the loss of perfect tracking at low Y in Figure 2B. On the other hand, at high Y values, excess X_C is produced and the function $\beta_P \frac{\mu K_C}{\mu K_C + \theta X_C}$ has a small effective value. In this regime, proportional feedback is lost, and the system acts like an I control scheme (Figure 2B, right panel). As a result, while this function is effective in a range of operation centered around μK_C, this dynamic range is limited.

A simple upgrade to include dependence both on Y and X_C uses the function $f_P(X_C, Y) = \beta_P \frac{\mu Y}{\mu Y + \theta X_C}$. This function has the advantage that it scales with the reference set-point Y, allowing for a larger dynamic range before saturation. The result is better tracking at low Y and improved damping following perturbations in the parameters of the controlled process such as β_C (Figure 2C). This implementation, however, still

(B–D) Time dynamics of output $X_C(t)$ for different proportional control f_P functions (PI control, $D_t(X_C, Y) = 0$). (B) Michaelis-Menten function dependent negatively on X_C. (C) Michaelis-Menten function dependent negatively on X_C and postively on the set-point Y. (D) Michaelis-Menten function dependent negatively on X_C and postively on the set-point Y with maximum synthesis rate dependent on Y. For the f_P functions tested, their parameters were chosen so that all f_P functions had the same value for a chosen set-point value of $Y = 300$ nM and the same effective proportional weight k_P (see Section "Linear perturbation analysis of nonlinear PID control design provides analytical support for the design" for derivation of k_P) at $Y = 300$ nM ensuring identical adaptation dynamics. See Table S1 for parameter values used in each simulation.

incurs a steady-state error from the desired $X_{C_{ss}} = \mu Y/\theta$ at low Y because of the basal production of X_C and Z_2 in this regime, similar to the prior proportional function. Here, again, the I control is not active until Y is high enough to engage it. At high values of Y, stable oscillations still emerge due to loss of P control.

We propose the following proportional control strategy that accommodates both low and high Y regimes:

$$f_P(X_C, Y) = \beta_P Y \frac{\mu Y}{\mu Y + \theta X_C} \quad \text{(Equation 9)}$$

At low Y values, $f_P(X_C, Y)$ is proportionally low, reducing the basal synthesis of X_C and Z_2 accordingly and ensuring that I control is still active. This restores tracking at low Y values (Figure 2D, left panel). At high Y values, $f_P(X_C, Y)$ also scales accordingly, maintaining the relative contribution of the proportional term to the control system and resulting in improved damping (Figure 2D, right panel).

The function $f_P(X_C, Y)$ from Equation 9 can be rearranged to give

$$f_P(X_C, Y) = \frac{\beta_P}{2\mu}\left(\mu Y + \frac{\mu Y}{\mu Y + \theta X_C}[\mu Y - \theta X_C]\right) \quad \text{(Equation 10)}$$

This rearrangement reveals a dependence on the error $e(t) = \mu Y - \theta X_C(t)$, which is multiplied by the ratio $\frac{\mu Y}{\mu Y + \theta X_C}$ and shifted by Y in order to maintain a positive quantity. The improved performance of this functional form of proportional control hinges on this dependence. This is further vetted by analytical arguments presented below in Section "Linear perturbation analysis of nonlinear PID control design provides analytical support for the design." A possible experimental realization of this function relies on competitive binding to a regulated promoter between X_C and a transcription factor whose activity is proportional to Y. This design is discussed in STAR Methods "Experimental realization of proportional control function" and Figure S2A.

Finally, we note that although we presented our argument using a function of the form $f_P(X_C, Y) = \beta_P Y \frac{\mu Y}{\mu Y + \theta X_C}$ that is positioned at $\beta_P Y/2$ when the system is at steady state, our analyses still hold for other less tuned functions. For example, Equation 9 is derived from a more general biochemical function $f_P(X_C, Y) = \beta_P Y \frac{\alpha_P Y}{\alpha_P Y + X_C + \varepsilon_C}$ (STAR Methods "Experimental realization of proportional control function"). When $\alpha_P = \mu/\theta$ and $\epsilon_C = 0$, the two functions are the same. If $\epsilon_C > 0$, f_P (X_C, Y) is a weaker proportional feedback function, but this can be compensated by increasing the value of β_P accordingly (Figure S2B). Likewise, if $\alpha_P \gg \mu/\theta$, f_P (X_C, Y) is close to $\beta_P Y$ at steady state, and the system saturates for negative swings in X_C. For $\alpha_P \ll \mu/\theta$, f_P (X_C, Y) is a small quantity with very little sensitivity. Here again, these deviations can be compensated for by adjusting the proportional control weight β_P (Figure S2C). However, this benefit of increasing β_P is not unlimited. For a given β_I, increasing β_P excessively beyond a certain value may drive Z_1 to be too low to be able to control Z_2, therefore undermining the controller (see Figures S1C and S1F and STAR Methods "Bounds on antithetic integral control with P and D terms" for analysis of this case pertaining to the antithetic integral controller). Further design options can be deployed to alleviate this effect. For example, adding an active degradation term to the X_1 equation, Equation 8, can extend the range of β_P (and the range of process parameter values) for which the integral controller remains operational (see STAR Methods "Adding active degradation to the X_1 equation," and Figure S3). In either case, as with any control design and given a process and its parameters, the control weights β_I and β_P need to be iteratively determined to avoid regimes where the integral controller is inoperable.

Design of a Derivative Control Term

To design a derivative control term, we drew inspiration from bacterial chemotaxis in which a bacterium's sensing and adaptation circuit is capable of measuring time derivatives of chemoattractant concentrations as the bacterium swims up or down a gradient (Barkai and Leibler, 1997). To generate a simple implementation, we adopted a simplified 2-node circuit of the process from Ma et al. (Ma et al., 2009). Adapting this circuit to our purposes, we propose the following interactions in a dynamical system that can perform an approximate time derivative measurement of X_C, through the following equations:

$$\frac{dA}{dt} = \beta_A M - \gamma_A X_C \frac{A}{K_A + A} - \gamma_{A_0} A \quad \text{(Equation 11)}$$

$$\frac{dM}{dt} = \beta_M Y - \gamma_M A \frac{M}{K_M + M} \quad \text{(Equation 12)}$$

The derivative control term proposed for Equation 8 is then given by $D_t(X_C, Y) = \beta_D A$, where A is the output of the derivative motif in Equations 11 and 12. This circuit consists of two molecules, A and M, where A is produced at a rate proportional to M and actively degraded by X_C. M is produced at a rate proportional to the reference signal Y (the signal to be tracked by the controlled process) and actively degraded by A. One requirement for the derivative computation through this circuit is that the active degradation terms (Michaelis-Menten functions) operate at or near saturation with $K_A \ll A$ and $K_M \ll M$, over the range of set-point values desired of the process. This results in the following approximate equations:

$$\frac{dA}{dt} \approx \beta_A M - \gamma_A X_C - \gamma_{A_0} A \quad \text{(Equation 13)}$$

$$\frac{dM}{dt} \approx \beta_M Y - \gamma_M A \quad \text{(Equation 14)}$$

To see how the time-derivative measurement of X_C is achieved, we start by taking the time-derivative of Equation 13, solving for $\frac{dM}{dt}$ and substituting the resulting expression into Equation 14, which yields

$$\frac{d^2A}{dt^2} + \gamma_{A_0}\frac{dA}{dt} + \beta_A \gamma_M A \approx -\gamma_A \frac{dX_C}{dt} + \beta_A \beta_M Y \quad \text{(Equation 15)}$$

Since A and M are design variables, their parameters can be chosen so that there is a desired timescale separation between their dynamics and those of X_C (t). If one views X_C (t) as an input signal with many frequencies to the derivative motif, the parameters γ_{A0}, β_A, and γ_M of the derivative motif can be chosen so that its dynamics are faster than the highest frequencies of the X_C (t) signal. Specifically, if we define a frequency ω_{max} as the upper frequency bound of, for example, 99% of the frequency

content of X_C, representing an upper-bound on the fastest timescales of X_C, then the parameters of the derivative motif can be chosen such that $\left|-\omega_{max}^2 + \gamma_{A_0} j\omega_{max}\right| \ll \beta_A\gamma_M$ (STAR Methods "Realizing the derivative control term"). Evidently, the maximal frequency ω_{max} of X_C is that of the closed loop system, which is dependent on the parameters and the inputs. It would change over the course of adjusting the control gains (β_I, β_P, β_D), but an iterative procedure can be used to refine the estimate of these gains and derivative parameters (STAR Methods "Realizing the derivative control term").

Applying the timescale separation above, i.e., $\left| - \omega_{max}^2 + \gamma_{A_0} j\omega_{max}\right| \ll \beta_A\gamma_M$, we then obtain the following approximate tracking relationship from Equation 15 between the inputs X_C and Y and the output A

$$A \approx -\frac{\gamma_A}{\beta_A\gamma_M}\frac{dX_C}{dt} + \frac{\beta_M}{\gamma_M}Y \qquad \text{(Equation 16)}$$

Effectively, Equation 16 shows that A is proportional to the negative time derivative of the input X_C plus a steady-state value that scales with the reference Y, a result also reproduced by the simulations of Figures S4 and 3A. This relationship neglects brief fast scale dynamics that occur following step changes in $Y(t)$, which contain higher frequencies that violate the condition $\left| - \omega_{max}^2 + \gamma_{A_0}\omega_{max}\right| \ll \beta_A\gamma_M$. In this case, the derivative motif will exhibit a fast transient before accurate tracking of $dX_C(t)/dt$ occurs. Such transient dynamics can also occur for step changes in the process parameters as well as in the parameters of the derivative motif itself. Our simulations and results, however, always use Equations 11 and 12, which capture all dynamics, slow and fast.

As with proportional control, the addition of a derivative term to the I control improves its transient response to step Y inputs and perturbations in β_C (compare Figures 3C and 2A). Also, like proportional control, the fact that A in Equation 16 scales with Y is crucial for the motif to measure the time derivative of X_C over a large dynamic range. To illustrate this point, we compare an integral-derivative (ID , $f_P(X_C, Y) = 0$) controller in which the production rate of M in the derivative calculation motif does not scale with Y to the design in which it does (Equation 12). The derivative controller that lacks explicit dependence on Y also causes loss of perfect tracking (Figure 3B, left panel) and adaptation (Figure 3B, right panel, and Figure S1B) at low Y levels. Here again, the I control is not active until Y is high enough to engage it. At high levels of Y, oscillations also appear for perturbations in β_C. By contrast, basal production at low Y and oscillations at high Y do not manifest if the synthesis rate of M in the derivative control design scales with Y (Figure 3C).

Having explored I , PI and ID control, we can now combine all three terms to obtain PID control. Figure 3D shows how the inclusion of both P and I also improves performance in a manner that is similar to that of the PI and ID cases (Figures 2D and 3C, respectively). However, here again, care should be taken in picking the values of the proportional weight β_P and derivative weight β_D. If they are too large compared for a given β_I, these control terms might undermine the integral control (Figures S1C, S1D, and S1E). To assess the relative contribution of the different control terms to controller performance, we explored adaptation times of the output of the closed loop system for different values of the control weights following a disturbance in β_C (Figure S5). For this simple process, the P and the D showed a relatively additive benefit (inverse relationship in the heatmap), indicating that in this case, any one of them can be used alone to maximum benefit for this performance criterion. In Section "PID benefits depend on the process to be controlled and PID gains need to be tuned," we further explore how the integral and derivative terms affect the performance of the PID controller applied to a more complicated process, illustrating that different processes that need to be controlled require a different constellation of controller choices.

Thus far, we have neglected dilution due to cell division, which can introduce some error in set-point tracking (Qian and Del Vecchio, 2018), due to $\gamma_d Z_1$ and $\gamma_d Z_2$ appearing in Equations 6 and 7, respectively, for a non-zero dilution rate γ_d. When we include dilution for the I, PI, and ID cases from Figures 2A, 2D, and 3C, respectively (see Figure S6), we get an expected error in tracking the set point for the I case. However, the addition of P and D terms helps reduce this error. This is because the P and D terms reduce the steady-state levels of Z_1. For the remainder of the paper, we return to the assumption that dilution is zero.

Perturbation Analysis of Nonlinear PID Control Design Provides Analytical Support for the Design

To provide an analytical interpretation for the proposed PID controller, we apply linear perturbation analysis to Equations 6, 7, 8, 9, 11, and 12. Even though the simulations above were for the particular controlled process in Equation 5, the linear analysis is presented for any general controllable process, allowing us to compare our design with a traditional textbook example of a linear PID system extensively used in engineering (Dorf and Bishop, 1995). In this case, we suppose that the purpose is to control a process whose output is $x_C(t)$ to a set point $r(t)$ (Figure 1B). That is, we want to drive the error $e(t) = r(t) - \theta x_C(t)$ to zero using a traditional linear PID controller. We will assume that $r(t) = \mu y(t)$ to make this example directly comparable with the biochemical PID controller.

A traditional PID controller uses an input $u(t)$ into the controlled process that consists of weighted sums of the error (P control, $k_P e(t)$), the integral of error (I control, $k_I \int e(t)d\tau$), and the time-derivative of error (D-control, $k_D\frac{de(t)}{dt}$) to correct deviations from desired set point (Figure 1B):

$$u(t) = k_P[\mu y(t) - \theta x_C(t)] + k_I\int_0^t [\mu y(\tau) - \theta x_C(\tau)]d\tau + k_D\left[\mu\frac{dy(t)}{dt} - \theta\frac{dx_C(t)}{dt}\right] \qquad \text{(Equation 17)}$$

A standard framework for analyzing a linear PID control system is through Laplace-domain and frequency-domain analysis (Dorf and Bishop, 1995). A Laplace transform translates time-domain signals, e.g., $x_C(t)$, to Laplace-domain signals $x_C(s)$, where s is the Laplace-domain variable related to frequency ω through the relationship $s = j\omega$, where $j = \sqrt{-1}$. Assuming zero disturbance ($d(s) = 0$), $x_C(s)$ is given

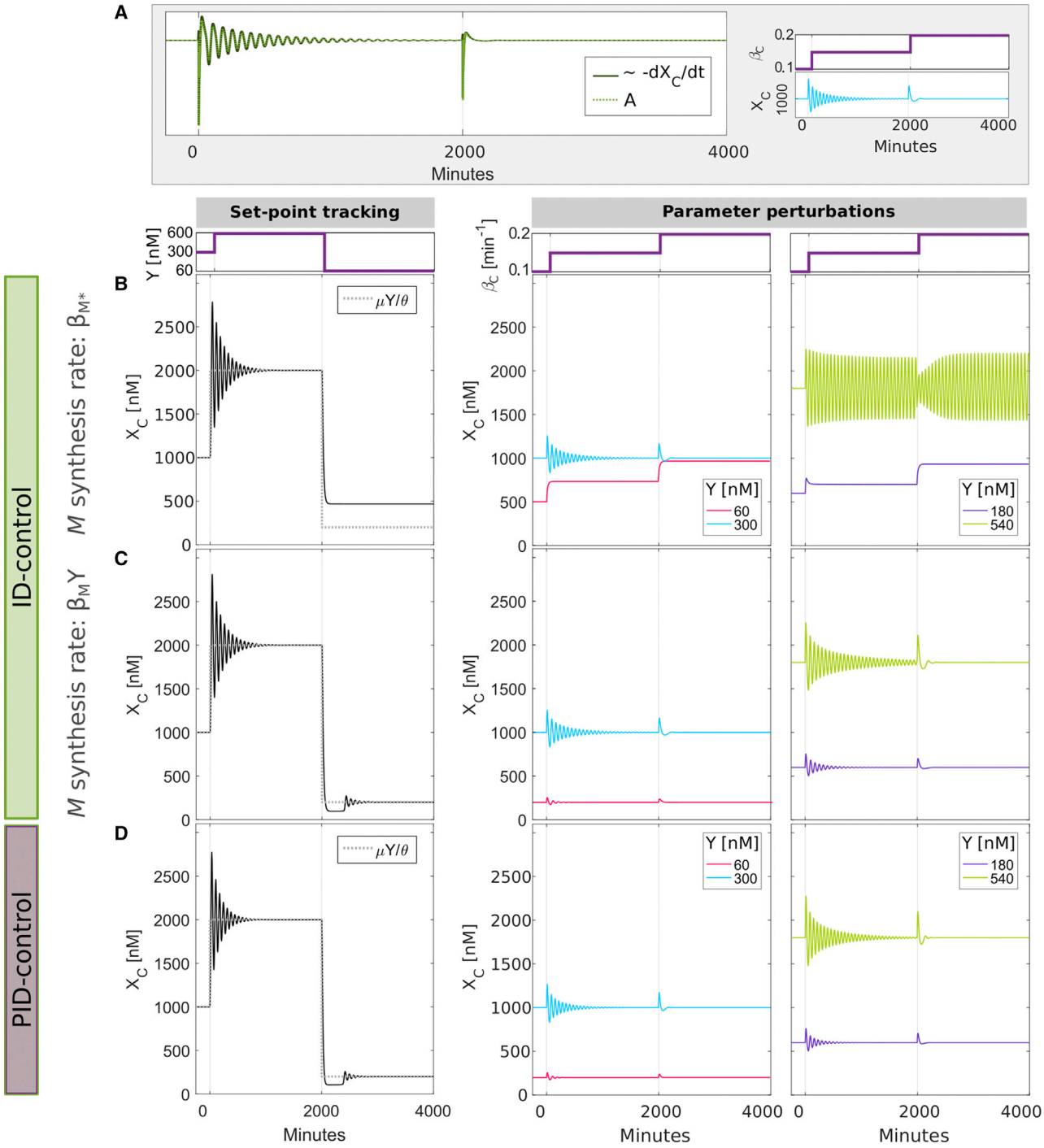

Figure 3. Integral-Derivative Control Can Produce Better Transient Dynamics than Integral Control Alone

(A) Time dynamics of A and a numerical approximation of $\frac{dX_C}{dt}$ for the derivative motif in Equations 11 and 12. Plots shown are for $Y = 300$ nM and perturbations to β_C (see inset).

(B) Time dynamics of output $X_C(t)$ following a change in the set-point Y (left panel) or in process parameter β_C (right panel). The outcome of β_C perturbation is also shown for different values of $Y = [60, 180, 300, 540]$ nM. Simulations are shown for process in Equation 5 and controller in Equations 6, 7, and 8 of main text with $f_P(X_C, Y) = 0$. Derivative function $D_t(X_C, Y)$ is given by $D_t(X_C, Y) = \beta_D A$, where A is the output of the derivative motif in Equations 11 and 12, except that in this case, the equation for M does not depend on set-point Y.

(C) Time dynamics of output $X_C(t)$ for full derivative control design in Equations 11 and 12 with dependence of M on set-point Y. Compare with Figure 2A (I only).

(D) Simulations for full PID controller under the same conditions as in (B) and (C). See Table S1 for parameter values used in each simulation.

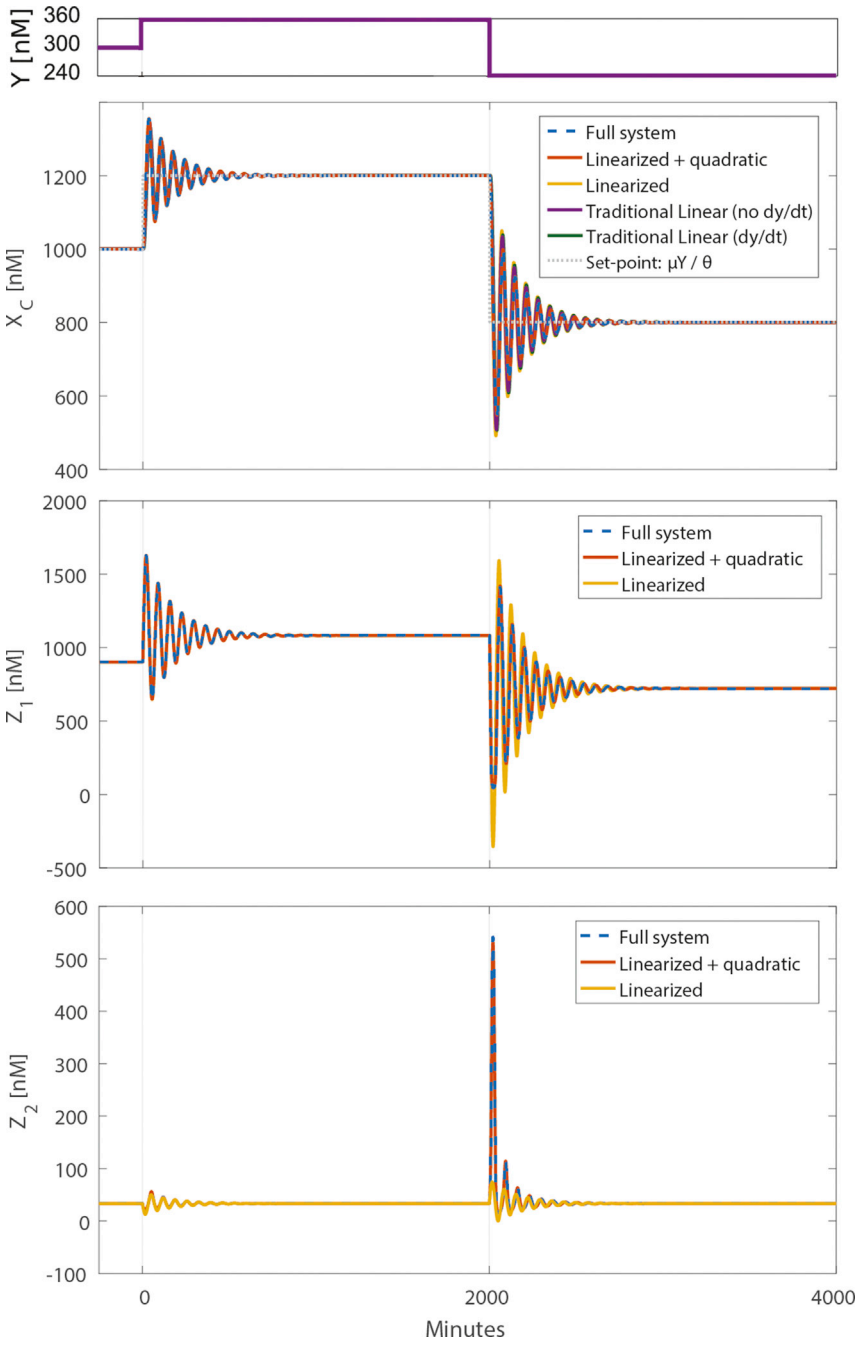

Figure 4. Comparison of Nonlinear PID Control to Its Linearized Equations in Response to Perturbations in Set-point *Y*

The time dynamics of X_C, Z_1, and Z_2 are plotted for the full model (dashed blue, Equations 5, 6, 7, 8, 11, and 12), the linearized model (orange, Equation S22), the linearized model plus quadratic correction term, $\eta z_1(t)z_2(t)$ (red), and the traditional linear PID (purple, Equation S28, no $k_D\mu\frac{dy}{dt}$ term; and green, Equation S28, $k_D\mu\frac{dy}{dt}$ term) for X_C only. *Y* values are shown in the top panel. See Table S1 for parameter values used in each simulation.

by $x_C(s) = u(s)\Phi(s)$, where $\Phi(s)$ is the process transfer function between the process input $u(s)$ (the action delivered by the PID controller) and $x_C(s)$ (Figure 1B). Simple calculations then show that the Laplace-domain relationship between $r(s) = \mu y(s)$ and $x_C(s)$ for a traditional PID controller is

$$x_C(s) = \frac{[k_I + sk_P + s^2k_D]\Phi(s)}{s + \theta[k_I + sk_P + s^2k_D]\Phi(s)}\mu y(s) \qquad \text{(Equation 18)}$$

In the Laplace domain, steady state is evaluated at $s = 0$. For the steady state to be stable, it is required that the real parts of the poles in Equation 18 are negative. Now assuming that $\Phi(s = 0) \neq 0$, the steady-state output $x_C(s = 0)$ is equal to $\mu y(s = 0)/\theta$, as required for perfect set-point tracking. This is of course only the case when k_I is non-zero, and therefore integral control is necessary.

Evidently, the biochemical controller we are proposing is nonlinear. But we can determine its local small-signal properties and relate them to the textbook framework above (Figure 1B; Equation 18) using linearization of Equations 6, 7, 8, 9, 11, and 12 around a steady state $\{X_{1_{ss}}, Z_{1_{ss}}, Z_{2_{ss}}, A_{ss}, M_{ss}, X_{C_{ss}}, Y_{ss}\}$ achieved for a desired set point. This traditional treatment (presented in detail in STAR Methods "The control circuit equations linearized about a set point") generates equations that hold locally for the behavior of the deviation $\{x_1(t), z_1(t), z_2(t), a(t), m(t), x_C(t)\}$ from the steady-state values as a result of small perturbations to the system. The total solution is the steady-state solution plus the perturbed solution; for example, the time-dependent solution for $X_C(t)$ would be $X_C(t) = X_{C_{ss}} + x_C(t)$. Likewise the input $Y(t)$ would be $Y(t) = Y_{ss} + y(t)$. Simulations of the linearized controller compared favorably to the nonlinear PID system for small to moderate perturbations (Figure 4 for set-point tracking, and Figures S7A and S7B for parameter perturbations). Evidently, bigger differences between linearized and nonlinear systems were present for larger perturbations. However, these differences were muzzled by adding the quadratic term $\eta z_1(t)z_2(t)$ of the antithetic reaction to the linearized system, suggesting that this is the most impactful nonlinearity in the design for the parameters used.

Using the linearized equations for the biomolecular controller, we can investigate how the transfer function between $y(s)$ and $x_C(s)$ compares with the traditional PID. The Laplace-domain transfer function of the linearized biochemical PID controller (see STAR Methods "The control

circuit equations linearized about a set point'' for derivation) is given by:

$$x_C(s) = \frac{\left[\beta_I \frac{s+\eta Z_{1_{ss}}}{s+\eta Z_{1_{ss}}+\eta Z_{2_{ss}}} + 3sk_P + \frac{\theta\beta_A\beta_M}{\gamma_A\mu} sk_D\right]\Phi(s)}{s+\theta\left[\beta_I \frac{\eta Z_{1_{ss}}}{s+\eta Z_{1_{ss}}+\eta Z_{2_{ss}}} + sk_P + s^2k_D\right]\Phi(s)} \mu y(s)$$

(Equation 19)

For the simple process model we have used so far (Equation 5), the transfer function between the process input $u(s)$ and $x_C(s)$ is $\Phi(s) = \frac{\beta_C}{(s+\gamma_1)(s+\gamma_C)}$. Evidently, at steady state, $x_C(s=0) = \mu y(s=0)/\theta$, consistent with the full nonlinear system. In this function, k_P is the proportional control gain and k_D is the derivative control gain, which are given by $k_P = \frac{\beta_P}{4\mu}$ (with $k_P = \frac{\beta_P}{\alpha_P\theta}\frac{(\alpha_P)^2}{(\alpha_P+\mu/\theta)^2}$, for $\alpha_P \neq \mu/\theta$ in a general proportional term), and $k_D = \frac{\beta_D}{\theta}\frac{\gamma_A}{\beta_A\gamma_M}$, respectively.

While k_D and k_P only depend on parameters and are therefore constant, the integral gain terms in the numerator and denominator of Equation 19 are a function of the Laplace-domain variable s. As a result, the linearized antithetic integral control does not exactly map onto a mathematical representation of a traditional linear integral controller. However, these two representations converge under clear constraints on the timescale of the integral controller. Specifically, if ω_{max}, defined as the upper frequency bound of 99% of the frequency content of $x_C(s)$ in the closed loop system, is such that $|s_{max}| = |j\omega_{max}| \ll \eta Z_{1_{ss}}$, then the function $\beta_I \frac{s+\eta Z_{1_{ss}}}{s+\eta Z_{1_{ss}}+\eta Z_{2_{ss}}}$ is almost constant over all frequencies below ω_{max}. Specifically, when this requirement is met then $k_I \approx \frac{\beta_I Z_{1_{ss}}}{(Z_{1_{ss}}+Z_{2_{ss}})}$. Mechanistically, this could be achieved if binding of the two antithetic molecules that constitute the integral control is much faster than the dynamics of the transcriptional process to be controlled, and this approximation also improves with increasing Y, which corresponds to increasing $Z_{1_{ss}}$ (see STAR Methods ''The control circuit equations linearized about a set point'' and Figure S7C). Substituting k_I into the transfer function in Equation 19 becomes

$$x_C(s) \approx \frac{\left[k_I + 3sk_P + \frac{\theta\beta_A\beta_M}{\gamma_A\mu} sk_D\right]\Phi(s)}{s+\theta[k_I + sk_P + s^2k_D]\Phi(s)} \mu y(s) \qquad \text{(Equation 20)}$$

In this approximate transfer function, k_I, k_P, and k_D are now all constants, and the similarities between this equation and that of the traditional PID controller in Equation 18 become clear. Equation 20 has the same denominator (poles of the transfer function) as the traditional PID controller in Equation 18). But, the two expressions have different numerators (zeros for the transfer function). First, there is a difference in the numerator term that multiplies the proportional gain (sk_P versus $3sk_P$). The proportional control term in a traditional PID controller acts on the standard tracking error (i.e. $k_P(\mu y - \theta x_C)$ in this case). The structure of Equation 9 generates a linearized proportional control function that acts on a different quantity, manifesting as $3k_P\mu y - k_P\theta x_C$, which is at the root of the difference in the proportional term. This multiplicity of the term $k_P y$ is in fact the result of Y appearing in multiple places in Equation 9, which leads also to multiplicity in the linearization (see STAR Methods ''The control circuit equations linearized about a set point'').

Second, the term that multiplies the derivative gain in the biochemical design is given by $\frac{\theta\beta_A\beta_M}{\gamma_A\mu} sk_D$, while its counterpart in a traditional design would be s^2k_D. This difference can be explained by the fact that the derivative control term in a traditional PID controller acts on the tracking error, i.e. $k_D\left(\mu\frac{dy}{dt} - \theta\frac{dx_C}{dt}\right)$, while as we discussed above, the biomolecular implementation of derivative control computes a scaled form of $\frac{dx_C}{dt}$ that is also dependent on the reference Y, but not its derivative (see Equation 16. For the simple process simulated in Figure 4, the linearized biochemical PID controller showed similar properties as the traditional linear PID controller for set-point tracking (Figure 4A) and parameter perturbations (Figures S7A and S7C, Section ''The control circuit equations linearized about a set point''). Indeed, for this system, the presence of a $k_D\mu\frac{dy}{dt}$ term (that is, having an s^2k_D in the numerator of the transfer function) has an insignificant effect on set-point tracking. This is of course not true for more complex processes, and we show in Section ''PID benefits depend on the process to be controlled and PID gains need to be tuned'' that for one such process, the presence of a $k_D\mu\frac{dy}{dt}$ term (and hence a full dependence of the derivative term on the tracking error) improves set-point tracking dynamics. If this improvement is required for the desired application, a modified version of our D motif can be considered, which can add an s^2k_D term in the numerator of Equations 19 and 20 above, but at the cost of increased biochemical complexity (see STAR Methods ''An alternative derivative motif'' and ''Linearized analysis of the alternative derivative motif'' for details).

It is useful to note here, however, that while the s^2k_D term is relevant to set-point tracking, it is not relevant for adaptation to parameter perturbations. This can be seen from Equation 20, where the input of the linearized biochemical controller $u(t)$ to the process is

$$u(t) = k_P[3\mu y(t) - \theta x_C(t)] + k_I\int_0^t [\mu y(\tau) - \theta x_C(\tau)]d\tau + k_D\left[\frac{\theta\beta_A\beta_M}{\gamma_A\mu}\mu y(t) - \theta\frac{dx_C(t)}{dt}\right]$$

(Equation 21)

For step changes in process parameter values, in which the change in input is $\mu y(t) = 0$, the controller input $u(t)$ is identical for both the traditional and biochemical PID (compare Equations 17 and 21 for $\mu y(t) = 0$). Therefore, they control a given process in the same way upon perturbations to process parameter values (further discussion of this comparison is given in STAR Methods ''The control circuit equations linearized about a set point'' with examples in Figure S7C).

Finally, Equation 20 and the expressions derived for the effective k_I, k_P, and k_D provide an analytical framework to discuss the differences in behavior seen for different implementations of the proportional feedback mechanism of Section ''Design of a proportional control term.'' As mentioned above, k_P is constant across set points for our proposed design of proportional feedback, at least in the linearized regime. For other proportional

functions that were tested and generated narrower dynamic range, that is for $\beta_P \frac{(\mu K_C/\theta)}{(\mu K_C/\theta)+X_C}$ and $\beta_P \frac{(\mu Y/\theta)}{(\mu Y/\theta)+X_C}$, the linearized proportional gains are given by $k_P = \beta_P \frac{(\mu K_C/\theta)}{\theta((\mu K_C/\theta)+\mu Y_{ss}/\theta)^2}$ and $k_P = \frac{\beta_P}{4\mu Y_{ss}}$, respectively. For both cases, k_P decreases to zero as Y increases, indicating that k_P becomes insignificant at higher Y, leaving only an I control like behavior (compare Figures 2A–2C, right panel). For low Y, where these proportional functions caused basal levels of X_C, the integral control is not active and Z_2 grows at a positive constant rate since Z_1 is too low to contribute to its annihilation (see Figure S1A). While the other variables in the system reach a steady state, the increasing level of Z_2 causes Z_1 and $k_I \approx \beta_I Z_1/(Z_1+Z_2)$ to go to zero, i.e., the integral controller is broken and has no effect on the system. Thus, the system loses perfect tracking and adaptation capabilities. These analytical considerations, therefore, further support the conclusions reached by numerical analysis of the control system in its nonlinear operation (Figures 2D and 3C).

They allow us, in addition, to explore questions about control theoretic properties of the biochemical controller that could be inferred through its quantitative resemblance to the traditional PID controller. For example, the transfer functions of the two controllers only differ in their k_I, with $k_I = \beta_I \frac{Z_{1ss}}{Z_{1ss}+Z_{2ss}}$ for the biochemical controller. As a result, we can infer that if the traditional controller is stabilizing of a given process for $k_I = \beta_I$ and for smaller k_I, then the biochemical controller is also stabilizing. Other properties can also be explored using this linearization framework, a fertile ground for future research.

PID Benefits Depend on the Process to Be Controlled and PID Gains Need to Be Tuned

To move our analysis beyond a simple process that only contains a simple transcriptional step, we consider a more general multi-step process connecting X_1 to X_C with negative feedback defined by the following equations

$$\frac{dX_{D_1}}{dt} = \frac{N}{\tau_D}X_1 - \frac{N}{\tau_D}X_{D_1} - \gamma_F X_C \frac{X_{D_1}}{X_{D_1}+K_F} \quad \text{(Equation 22)}$$

$$\frac{dX_{D_i}}{dt} = \frac{N}{\tau_D}X_{D_{i-1}} - \frac{N}{\tau_D}X_{D_i} \quad \text{(Equation 23)}$$

$$\frac{dX_C}{dt} = \beta_C X_{D_N} - \gamma_C X_C \quad \text{(Equation 24)}$$

for $2 \le i \le N$, and with X_1 still given by Equation 8. The multi-step process between X_1 and X_C has a mean response time of τ_D broken into N steps.

We now consider two specific process examples. First, when $\gamma_F = 0\ \text{min}^{-1}$, $\tau_D = 20$ min, $N = 2$, we obtain a process in which the open loop response for a step change in Z_1 monotonically increases to its new steady state and does not contain oscillations (Figure 5A). Second, for $\tau_D = 40$ min, $N = 4$, and $\gamma_F = 0.2\ \text{min}^{-1}$, we generate a process in which a negative feedback loop from X_C onto X_{D_1} exists. In this case, the open loop process response exhibits damped oscillations (Figure 5B). We explore the benefits of introducing feedback control for the two processes. For the first process, a tuned PI controller can achieve a dynamic response with almost no overshoot (Figure 5A, bottom plot, blue curve). Increasing k_I in this PI controller is detrimental as it adds some overshoot (Figure 5A, bottom plot, red curve) that cannot be corrected by adding a derivative control term (Figure 5A, bottom plot, orange curve). By contrast, for the second process, even a tuned PI controller still generates a closed loop response with a slow oscillating convergence to the set point (Figure 5B, bottom plot, blue curve). Here, however, addition of a derivative control term improves this transient performance (Figure 5B, bottom plot, orange curve). A thorough investigation of this system as a function of the control weights indicates that ID control is an adequate choice (Figure 6).

Finally, changing the input to the derivative motif from X_C to $X_C/(\mu Y + \theta X_C)$ achieves an approximate $k_D\frac{dy}{dt}$ term in the biochemical derivative controller, whose linearization now yields an output that is proportional to $\mu dy/dt - \theta dx_C/dt$, the time derivative of the error (see STAR Methods "An alternative derivative motif" and "Linearized analysis of the alternative derivative motif" for details). Evidently, this term increases the complexity of the derivative motif, but its application significantly reduces overshoot and improves the convergence rate relative to having no $k_D\frac{dy}{dt}$ term (Figure 5C, left panel). As explained above, this additional term does not impact adaptation to changes in process parameters (Figure 5C, right panel).

Taken together, these results indicate that the benefits of a full PID controller manifest differently for different biological processes and furthermore, that the contributions of the different feedback modalities also need to be tuned and refined based on the specific properties and timescales of the biological process to be controlled. This is similar to considerations that are routinely used in the design and implementation of control strategies in technological systems.

While we have demonstrated the applicability of the PID controller to an a example of a more complex process, more work needs to be done to demonstrate its applicability to very large-scale processes. In STAR Methods "Applicability of antithetic PID controller to arbitrary processes," and Figure S8A, we discuss the mathematical requirements to achieve this.

Constructing a PID Controller with a Different Integral Controller Architecture

We have so far exclusively designed and analyzed proportional and derivative control architectures that are used with the particular antithetic integral control strategy of Briat et al. (2016). However, given the additivity of the control terms in Equation 8, any input from a control design that can implement integral action can be readily used instead. For example, since the proportional control function f_P (X_C,Y) in Equation 10 has the tracking error encoded within, any biomolecular device that can integrate this function has the potential of implementing integral action, and can therefore, be used along with the P and D terms we proposed. To see this, let us assume that one can construct a variable Z that has a rate of change dictated by the following equation:

$$\frac{dZ}{dt} = \beta_Z Y \frac{\mu Y}{\mu Y + \theta X_C} - \gamma_Z Y \frac{Z}{Z+K_Z} \quad \text{(Equation 25)}$$

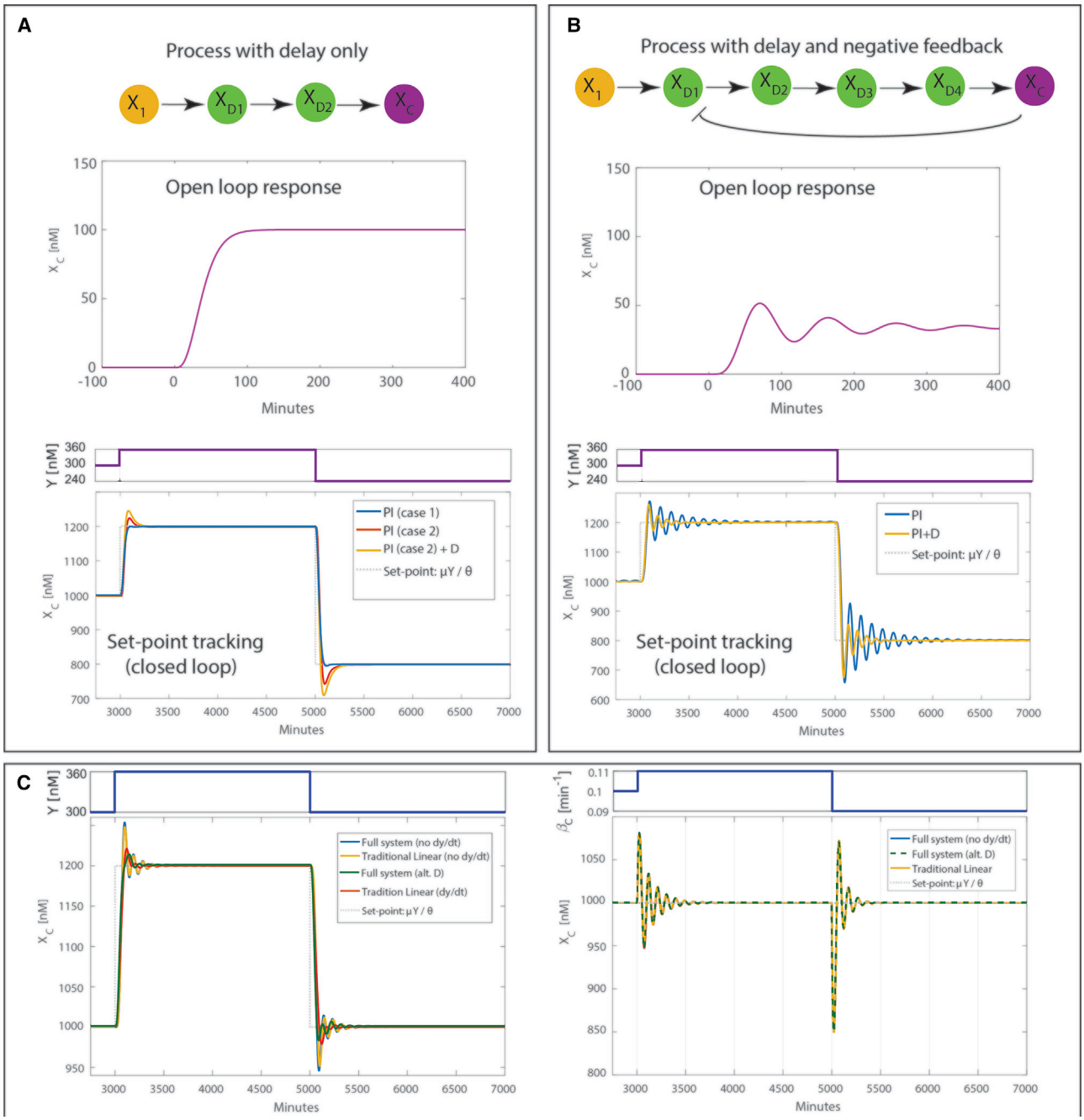

Figure 5. PID Benefits Depend on the Process to Be Controlled and PID Gains Need to Be Tuned Accordingly

(A and B) Top illustration shows a molecular diagram of the process to be controlled, middle plot shows the open loop response of a process to a step change in Z_1 (as defined in Figure 1A, but no feedback [$Z_2 = 0$]), and the bottom plot shows set-point tracking dynamics for different parameters of the feedback controller. (A) Process with $N = 2$, $\tau_D = 20$ min, and $\gamma_F = 0$ min^{-1}. Open loop response does not show pronounced oscillations. Tuned PI controller (case 1: with $k_I = 0.00375$, $k_P = 0.09$, and $k_D = 0$) generates set-point tracking with satisfactory dynamics. Change in k_I (case 2: $k_I = 0.0046$, $k_P = 0.09$, and $k_D = 0$) generates a larger transient response, and addition of derivative control term (case 2 + D: $k_I = 0.0046$, $k_P = 0.09$, and $k_D = 0.5$) does not lead to any improvement. (B) Process with $N = 4$ ($\tau_D =$ 40 min, and $\gamma_F = 0.2$ min^{-1}) and negative feedback. Open loop response shows damped oscillations. Tuned PI controller ($k_I = 0.02$, $k_P = 0.03$, and $k_D = 0$) generates set-point tracking with oscillations. Addition of a derivative control term (PI+D: with $k_I = 0.02$, $k_P = 0.03$, and $k_D = 4$) improves the transient response. (C) Plot of $X_C(t)$ as a function of time for different variations of derivative controller. Left plot: tracking following input set-point changes is improved in PID controllers with the addition of $k_D dY/dt$ term in an alternate derivative motif (see STAR Methods "An alternative derivative motif" and "Linearized analysis of the alternative derivative motif" for details). Right plot: response following a step change in a process parameter is very similar across PID controllers since their analytical expression coincide for this kind of perturbation.

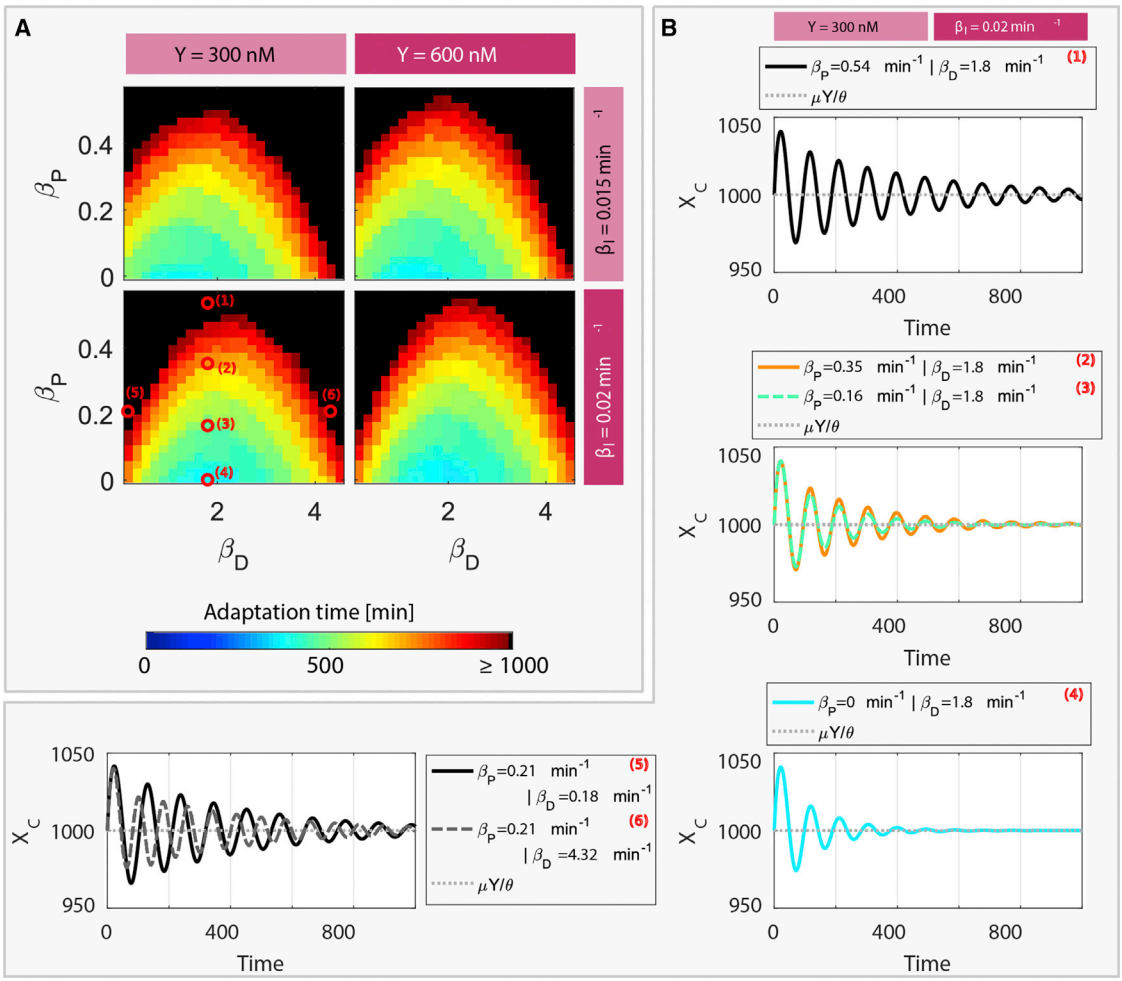

Figure 6. Adaptation Time as a Function of Control Weights for the Multi-step Process with Negative Feedback

(Second Example in Section "PID Benefits Depend on the Process to be Controlled and PID Gains Need to be Tuned" and Figure 5B).

(A) Plot of adaptation time as a function of control parameter weights. Each point on the heat map corresponds to a different value of β_P and β_D, and the color corresponds to the measured adaptation time according to the color-bar on the bottom. In each case a simulation is started from the steady states for β_C = 0.1 min^{-1}; the value of β_C is then changed to β_C = 0.15 min^{-1}, and the system simulated for 1,000 min. Following this perturbation to β_C, the system is assumed to have reached steady state once $X_C = \langle X_C \rangle \pm \varepsilon$, where $\langle X_C \rangle$ corresponds to steady state of X_C after the perturbation and ε is equal to 5% of the maximum observed "overshoot" or change with respect to $\langle X_C \rangle$ (see Figure S5A). The bin is in black if adaptation took too long (i.e. more than 1,000 min). Each panel shows adaptation for a different $Y = [300, 600]$ nM and $\beta_I = [0.015, 0.02]$ min^{-1} ; see Table S1 for all other parameter values used in these simulations. Numbers of plot correspond to parameter values further explored in (B).

(B) Examples of adaptation dynamics for different values of β_P and β_D, with Y = 300 nM and β_I = 0.02 min^{-1}. These examples map to the numbers shown on the lower left plot in (A). For this process, the ID controller achieves the best results.

In addition to the function $\beta_Z Y \frac{\mu Y}{\mu Y + \theta X_C}$ governing the production of Z, it is also actively degraded as a function of Y. Solving for X_C at steady state, Equation 25 becomes

$$X_{C_{ss}} = \left[\frac{\beta_Z}{\gamma_Z}\frac{Z+K_Z}{Z} - 1\right]\frac{\mu}{\theta}Y \qquad \text{(Equation 26)}$$

If this active degradation term (Michaelis-Menten function) also occurs at saturation ($K_Z \ll Z$), we then have the approximate steady-state equation.

$$X_{C_{ss}} \approx \left[\frac{\beta_Z}{\gamma_Z} - 1\right]\frac{\mu}{\theta}Y \qquad \text{(Equation 27)}$$

where one sees that $X_{C_{ss}}$ is proportional to Y, hence implementing perfect tracking. To ensure this relationship, in addition to the saturation constraint $K_Z \ll Z$, we are also constrained by the inequality $\frac{\beta_Z}{\gamma_Z} > 1$. This is required for the active degradation to be able to operate near saturation to enable integral control (see STAR Methods "Steady-State analysis of integral controller from Equation 25" and Figure S8B for analytical and graphical analysis).

To implement a PID controller, Z can then be input into the control of X_1 in the same fashion as Z_1 from the antithetic motif:

$$\frac{dX_1}{dt} = \beta_I^* Z + \beta_P Y \frac{\mu Y}{\mu Y + \theta X_C} + \beta_D A - \gamma_1 X_1 \qquad \text{(Equation 28)}$$

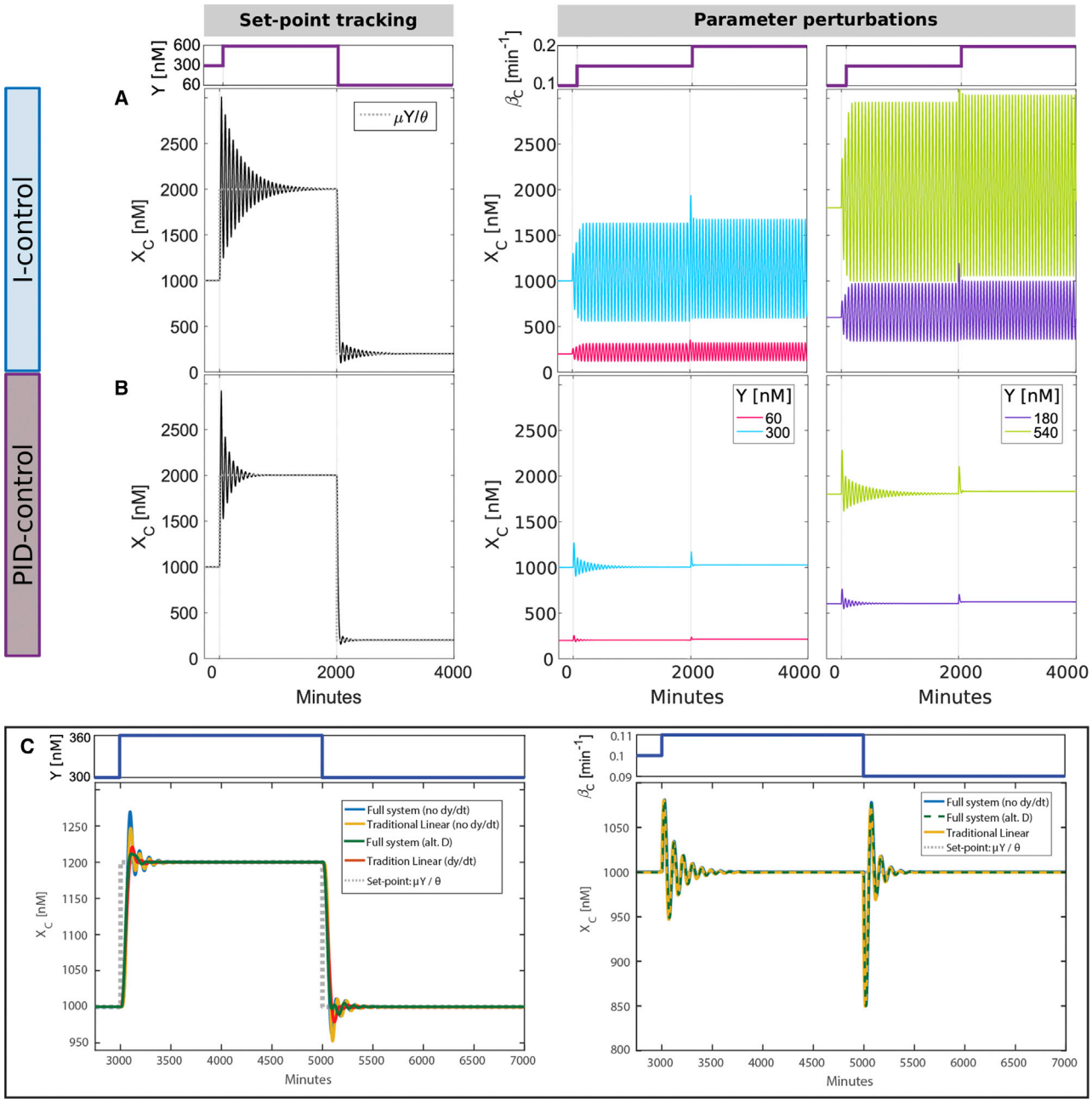

Figure 7. Proportional and Derivative Control Terms Improve Adaptation Dynamics Using a New Integral Controller Design

(A) Time dynamics of output $X_C(t)$ following a change in the set-point Y (left panel) or in process parameter β_C (right panel). The outcome of β_C perturbation is also shown for different values of $Y = [60, 180, 300, 540]$ nM. Simulations are shown for the process in Equation 5 and new integral controller design in Equations 25 and 28 (I control; $f_P(X_C,Y) = 0$ and $D_t(X_C,Y) = 0$).

(B) Time dynamics of output $X_C(t)$ with the addition of proportional and derivative control (PID control) using new integral controller design. Parameters used in (A) and (B) are listed in Table S1. (C) Time dynamics of output $X_C(t)$ with derivative control (ID control) using new integral controller design applied to the complex process simulated in Figure 5C. The new integral controller uses the same value of k_I as that simulated in Figure 5C with all other parameters of the integral controller being the same as in (A) and (B).

We investigated the use of this new integral controller design as a stand-alone, or in PID configurations (replacing Equations 6, 7, and 8 with Equations 25 and 28). To compare this new design with the antithetic design, we enforced $\frac{\beta_Z}{\gamma_Z} = 2$, which preserved $X_{C_{ss}} = \mu Y/\theta$. In the linearized regime, and unlike the antithetic controller, the new design generated a constant integral weight $k_I = \frac{\beta_I^* \beta_Z}{4\mu}$ (for derivation of k_I for this new PID see STAR Methods "Linearized analysis of the integral controller from Equation 25"), which we set to be equal to the highest generated control weight of the antithetic design. The values for the

proportional and derivative controller were kept unchanged, and thus, both designs share the same k_P and k_D. For all perturbations tested, applied to the simple process (Equation 5) , the new integral controller exhibited the same properties as the antithetic implementation (Figure 7A), and its performance was improved by addition of the proportional and derivative control terms (Figure 7B). The new integral controller also generated similar properties as the antithetic implementation when applied to the complex process of Figure 5C (Figure 7C). Taken together, these results indicate that the PID design we propose is modular, and that swapping implementations can be readily done as more designs emerge and are adopted.

DISCUSSION

We present in this work a design schema for a biology-specific PID controller. PID control has been one of the main workhorses of modern engineering, delivering facile, modular, and tunable control for many applications that we encounter in our everyday life, for example, the thermostat in our homes. A biochemical PID control strategy endowed with the same properties might also prove to be a general enabling technology for many synthetic biology applications. Our launching design was that for an integral (I) control strategy based on a simple antithetic relationship between two molecules developed by Briat et al. (2016), which we updated with newly designed biochemical proportional (P) and derivative (D) controllers. Much like their technological counterparts, these additional control terms alleviate the stability constraints of the use of integral control alone, and provide a malleable and tunable platform to modulate transient dynamics of a controlled system, for example, damping down or shortening oscillations. Importantly, through analytical methods, we could relate these designs directly to a traditional formulation of a PID controller, an analogy that facilitates the design and analysis of the biochemical controller based on established theories and practices in other fields. An important feature of the design we propose is its modularity, which we illustrate by exploring PI and ID designs as stand-alone possibilities, and also by swapping the antithetic integral controller with a new implementation inspired by the proportional design strategy (Section "Constructing a PID controller with a different integral controller architecture"). These properties might prove to be essential for applications in metabolic engineering and cellular therapeutics where different considerations and tradeoffs might be at play, and hence different combinatorial variations of the three terms (P, I, or D) might be needed and appropriate. They also might facilitate mixing and matching our designs with those of others, for example using implementation of a naturally occurring derivative motif that was recently analyzed (Hancock et al., 2017) and shown to exhibit excellent noise suppression characteristics at high frequencies.

While this paper presents a crucial first step for designing these control motifs, further analysis is needed to allow for their efficient and predictable use. For example, here we only considered a deterministic treatment of the biochemical controllers and processes to be controlled. Biochemical reactions are, of course, stochastic, and it is well known that the behavior of a single cell can diverge significantly from that of the population average. As a result, the deterministic analyses we present should be followed with thorough stochastic analyses to indicate when the two behaviors diverge and provide further guidance for the use of these controllers under conditions where stochastic effects dominate (Briat et al., 2016). In addition to probabilistic effects of biochemical reactions, it is also often the case that cells experience large variability in their general characteristics, for example, in the abundance of proteins. With this in mind, we investigated in this work the effect of parameter perturbations as a proxy, exploring when and how our controllers are able to tackle such changes. The analyses we present are evidently not exhaustive, and much work would need to be devoted to test the robust operation of the controllers we propose to such meaningful sources of variability. More analyses are also needed to determine the extent to which the controllers we propose are able to accomplish various control specifications, for example, the accurate tracking of a time-varying input signal Y.

While the work we report here presents a design for a general biochemical PID controller, as well as plausible suggestions in terms of molecular building blocks, a robust infrastructure needs to be developed in order to accelerate their implementation and testing. For example, design and implementation of a PID controller for technological systems usually proceeds by experimenting on the system to be controlled in order to determine its properties and hence the controller parameters that might be the most suitable. In our case, the success of the controller design relies on identifying the slower timescale of the process and positioning clearly defined parameters of the proportional and derivative controller accordingly. Often time, controller parameters are also fine-tuned in real time during system operation. Carrying out the same process for a biological controller is a formidable challenge, given the long timescales required to build and test in a cell a large number of control strategies or parameter variants. We are hopeful that progress in cellular engineering, as well as more studies that tackle efficient system identification in biological systems, will make this cycle more productive, proceeding on timescales that are compatible with rapid deployment of these technologies to various applications.

STAR★METHODS

Detailed methods are provided in the online version of this paper and include the following:

- KEY RESOURCES TABLE
- LEAD CONTACT AND MATERIALS AVAILABILITY
- METHOD DETAILS
  - Experimental Realization of X_1 Equation
  - Experimental Realization of Proportional Control Function
  - Adding Active Degradation to the X_1 Equation
  - Realizing the Derivative Control Term
  - Analysis of Poles in Equation S7
  - An Alternative Derivative Motif
  - The Control Circuit Equations Linearized about a Set-Point
  - Linearized Analysis of the Alternative Derivative Motif

- Linearized Analysis of the integral Controller from Equation 25
- Applicability of Antithetic PID Controller to Arbitrary Processes
- Z_1 Positively Regulates X_C in the Presence of P and D Terms
- Bounds on Antithetic Integral Control with P and D Terms
- Steady-State Analysis of Integral Controller from Equation 25

● DATA AND CODE AVAILABILITY

SUPPLEMENTAL INFORMATION

Supplemental Information can be found online at https://doi.org/10.1016/j.cels.2019.08.010.

ACKNOWLEDGMENTS

This work was supported by the Defense Advanced Research Projects Agency, contract no. HR0011-16-2-0045 to H.E.-S. The content and information does not necessarily reflect the position or the policy of the government, and no official endorsement should be inferred. H.E.-S. is a Chan-Zuckerberg investigator. A.H.N. was supported by the Department of Defense (DoD) through the National Defense Science & Engineering Graduate Fellowship (NDSEG) Program. We would like to thank the members of the El-Samad lab for fruitful discussions.

AUTHOR CONTRIBUTIONS

Conceptualization and methodology, M.C., M.G.-S., A.N., and H.E.-S.; Designed numerical experiments, M.C., M.G.-S., and A.N.; Performed the numerical experiments, M.C., M.G.-S.; Analyzed the data, M.C., M.G.-S., A.N., and H.E.-S.; Wrote the paper, M.C., M.G.-S., A.N., and H.E.-S.; Supervision and funding, H.E.-S.

DECLARATION OF INTERESTS

The authors declare no competing interests.

Received: May 9, 2018
Revised: March 14, 2019
Accepted: August 23, 2019
Published: September 25, 2019

REFERENCES

Alon, U., Camarena, L., Surette, M.G., Aguera y Arcas, B., Liu, Y., Leibler, S., and Stock, J.B. (1998). Response regulator output in bacterial chemotaxis. EMBO J. *17*, 4238–4248.

Aoki, S.K., Lillacci, G., Gupta, A., Baumschlager, A., Schweingruber, D., and Khammash, M. (2019). A universal biomolecular integral feedback controller for robust perfect adaptation. Nature *570*, 533–537.

Aranda-Díaz, A., Mace, K., Zuleta, I., Harrigan, P., and El-Samad, H. (2017). Robust synthetic circuits for two-dimensional control of gene expression in yeast. ACS Synth. Biol. *6*, 545–554.

Barkai, N., and Leibler, S. (1997). Robustness in simple biochemical networks. Nature *387*, 913–917.

Bennett, S. (1993). Development of the pid controller. IEEE Control Syst. *13*, 58–62.

Briat, C., Gupta, A., and Khammash, M. (2016). Antithetic integral feedback ensures robust perfect adaptation in noisy biomolecular networks. Cell Syst. *2*, 15–26.

Briat, C., Gupta, A., and Khammash, M. (2018). Antithetic proportional-integral feedback for reduced variance and improved control performance of stochastic reaction networks. J. R. Soc. Interface *15*.

Chae, T.U., Choi, S.Y., Kim, J.W., Ko, Y.S., and Lee, S.Y. (2017). Recent advances in systems metabolic engineering tools and strategies. Curr. Opin. Biotechnol. *47*, 67–82.

Dahl, R.H., Zhang, F., Alonso-Gutierrez, J., Baidoo, E., Batth, T.S., Redding-Johanson, A.M., Petzold, C.J., Mukhopadhyay, A., Lee, T.S., Adams, P.D., et al. (2013). Engineering dynamic pathway regulation using stress-response promoters. Nat. Biotechnol. *31*, 1039–1046.

Dorf, R.C., and Bishop, R.H. (1995). Modern control systems (Addison-Wesley).

El-Samad, H., Goff, J.P., and Khammash, M. (2002). Calcium homeostasis and parturient hypocalcemia: an integral feedback perspective. J. Theor. Biol. *214*, 17–29.

Francis, B.A., and Wonham, W.M. (1976). The internal model principle of control theory. Automatica *12*, 457–465. http://www.sciencedirect.com/science/article/pii/0005109876900066.

Goldbeter, A., and Koshland, D.E. (1981). An amplified sensitivity arising from covalent modification in biological systems. Proc. Natl. Acad. Sci. USA *78*, 6840–6844.

Hancock, E.J., Ang, J., Papachristodoulou, A., and Stan, G.B. (2017). The interplay between feedback and buffering in cellular homeostasis. Cell Syst. *5*, 498–508.e23.

Lim, W.A., and June, C.H. (2017). The principles of engineering immune cells to treat cancer. Cell *168*, 724–740.

Ma, W., Trusina, A., El-Samad, H., Lim, W.A., and Tang, C. (2009). Defining network topologies that can achieve biochemical adaptation. Cell *138*, 760–773.

Mangan, S., Itzkovitz, S., Zaslaver, A., and Alon, U. (2006). The incoherent feed-forward loop accelerates the response-time of the gal system of Escherichia coli. J. Mol. Biol. *356*, 1073–1081.

Muzzey, D., Gómez-Uribe, C.A., Mettetal, J.T., and van Oudenaarden, A. (2009). A systems-level analysis of perfect adaptation in yeast osmoregulation. Cell *138*, 160–171.

Purcell, O., Savery, N.J., Grierson, C.S., and di Bernardo, M. (2010). A comparative analysis of synthetic genetic oscillators. J. R. Soc. Interface *7*, 1503–1524.

Qian, Y., and Del Vecchio, D. (2018). Realizing 'integral control' in living cells: how to overcome leaky integration due to dilution? J. R. Soc. Interface *15*.

Strogatz, S.H. (2014). Nonlinear dynamics and chaos, Second edition (Westview Press).

Yi, T.M., Huang, Y., Simon, M.I., and Doyle, J. (2000). Robust perfect adaptation in bacterial chemotaxis through integral feedback control. Proc. Natl. Acad. Sci. USA *97*, 4649–4653.

STAR★METHODS

KEY RESOURCES TABLE

REAGENT or RESOURCE	SOURCE	IDENTIFIER
Software and Algorithms		
MATLAB	Mathworks	www.mathworks.com
MATLAB code used for all simulations and calculations	this study	https://github.com/mgschiavon/bioPIDcontrol

LEAD CONTACT AND MATERIALS AVAILABILITY

Further information and requests for resources should be directed to and will be fulfilled by the Lead Contact, Michael Chevalier (Michael.Chevalier@ucsf.edu).

METHOD DETAILS

Experimental Realization of X_1 Equation

A simple way to realize the sum of the control terms in Equation 8 is one in which every control action would result in the activation of a transcription factor that drives a different promoter, whose output is X_1. In this paper, these transcription factors are, Z_1 for the I term, T_P from Equation S3 for the P term, and A from Equation 11 and 12 for the D term. Therefore, the total X_1 would be the sum of the output of all three promoters. While there exist some synthetic promoters that may be applicable for this purpose (Aranda-Díaz et al., 2017), it is currently a non-trivial exercise to engineer and tune promoters.

Experimental Realization of Proportional Control Function

Here, we describe a design for realizing the proportional function $f_P(X_C,Y)$ from Equation 9 in main text. Many designs can achieve this function, but we focus on one that relies on technologies that are currently available (Aranda-Díaz et al., 2017).

The main building block in this design is an inducible transcription factor T_Y, which is constitutively expressed at high levels. In the absence of an activating ligand, this transcription factor resides outside the nucleus and it is therefore inactive. T_Y is, for example, a synthetic chimeric transcription factor that has an activating ligand binding domain (LBD) (Aranda-Díaz et al., 2017). In the presence of the cognate ligand, T_Y is activated and translocates to the nucleus where it activates a target promoter p_{TP}. We can modulate the level of active T_Y by adjusting the ligand concentration Y, predictably achieving a level of activated transcription factor T_{Y*} where $T_{Y*} = G_P Y$ (Aranda-Díaz et al., 2017).

We assume that T_{Y*} and the output of the process, X_C, can compete for a binding site at the promoter p_{TP} (see Figure S2A). At the promoter, either T_{Y*} is bound, X_C is bound, or neither is bound. Therefore, there are three possible promoter states, and transcription can occur only in the active T_Y-bound state (T_{Y*}). Assuming these binding events occur faster than transcription itself, the transcription rate of gene T_P can be computed to be:

$$H(X_C, T_Y) = \beta_0 \frac{R_P T_{Y*}}{R_P T_{Y*} + X_C + \varepsilon_P} \approx \beta_0 \frac{R_P G_P Y}{R_P G_P Y + X_C + \varepsilon_P} \quad \text{(Equation S1)}$$

R_P is the ratio of the dissociation constants of T_Y and X_C, and ε_P is the dissociation constant of X_C. Here we assume that T_Y and X_C have the same binding kinetics to p_{TP}. This assumption and the competition at the binding site can be achieved when T_Y and X_C are exactly the same transcription factor protein, but X_C has a crippled transcription activation domain. This can be readily achieved with modular synthetic transcription factors (Aranda-Díaz et al., 2017). In this case, $R_P \approx 1$. Either way, we set $R_P G_P = \alpha_P$ to get

$$H(X_C, T_Y) \approx \beta_0 \frac{\alpha_P Y}{\alpha_P Y + X_C + \varepsilon_P} \quad \text{(Equation S2)}$$

If we choose the minimum set-point to be $\alpha_P Y \gg \varepsilon_P$, then such a design would generate the first proportional function analyzed in the main text that scales with the input Y.

To realize the final proportional function, we further assume that the output of the motif above, T_P, is a transcription factor whose dynamics are governed by the equation:

$$\frac{dT_P}{dt} = H(X_C, T_Y) - \gamma_{T_P} T_P \quad \text{(Equation S3)}$$

If γ_{TP} has a fast decay rate, then $T_P \approx H(X_C, T_Y)/\gamma_{T_P}$. Like T_Y, T_P is a cytosolic (inactive) transcription factor that needs to be activated by a ligand to go into the nucleus. Here again, we can modulate externally the active T_P to be proportional to Y through changing ligand concentration, setting the activated transcription factor level to $T_P^* = F_P Y T_P = F_P Y H(X_C, T_Y)/\gamma_{T_P}$. If X_1 is now generated at a rate $\beta_n T_P^*$ by binding of T_P^* to a cognate promoter, then this generates the proportional control equation:

$$f_P(X_C, Y) = \frac{\beta_n F_P \beta_0}{\gamma_{T_P}} Y \frac{\alpha_P Y}{\alpha_P Y + X_C + \varepsilon_C} = \beta_P Y \frac{\alpha_P Y}{\alpha_P Y + X_C + \varepsilon_C} \quad \text{(Equation S4)}$$

Adding Active Degradation to the X_1 Equation

We add an active degradation term, $-\frac{\alpha_{\text{shift}}\beta_P Y}{2}\frac{X_1}{X_1 + K_{X_1}}$, for X_1 in Equation 8 in main text to get

$$\frac{dX_1}{dt} = \beta_I Z_1 + \left[\beta_P Y \frac{\mu Y}{\mu Y + \theta X_C} - \frac{\alpha_{\text{shift}}\beta_P Y}{2}\frac{X_1}{X_1 + K_{X_1}}\right] + \beta_D A - \gamma_1 X_1$$
$$= \beta_I Z_1 + \left[\frac{\beta_P Y}{2} + \frac{\beta_P}{2\mu}\frac{\mu Y}{\mu Y + \theta X_C}[\mu Y - \theta X_C] - \frac{\alpha_{\text{shift}}\beta_P Y}{2}\frac{X_1}{X_1 + K_{X_1}}\right] + \beta_D A - \gamma_1 X_1 \quad \text{(Equation S5)}$$

When this degradation proceeds at near saturation, that is $\frac{X_1}{X_1 + K_{X_1}} \approx 1$ and $\alpha_{\text{shift}} \approx 1$, then the proportional controller is not dependent on a shifted expression of the error since the term $\frac{\beta_P Y}{2}$ cancels out. For cases when perfect adaptation can be lost for the original controller upon perturbation to process parameter β_C (Figure S3A), it is maintained for the controller updated with this degradation term (Figure S3C). This occurs because in the first case, Z_1 becomes ineffective in this regime, while the addition of the degradation term extends the range of non-zero Z_1. These results suggest that including this additional term allows the system to endure larger positive changes in β_C (and β_P) before it loses integral control. It is important to note that while it is very difficult to perfectly tune α_{shift} to be exactly one, any non zero value for this parameter can provide some benefit (Figure S3B).

Realizing the Derivative Control Term

Here, we present details of Equation 16, the approximate time derivative representation of X_C from Section "Design of a derivative control term" in the main text. Transforming Equation 15 to the Laplace domain with Laplace-domain variable s yields

$$s^2 A(s) + \gamma_{A_0} s A(s) + \beta_A \gamma_M A \approx -\gamma_A s X_C(s) + \beta_A \beta_M Y(s) \quad \text{(Equation S6)}$$

and where $s = j\omega$ with ω being the frequency domain variable and $j = \sqrt{-1}$. Here we are enforcing that our initial conditions for $A(t)$ are zero, i.e. $A(t = 0^-) = 0$ and $dA(t = 0^-)/dt = 0$. Essentially, the system is off for $t < 0$ where $Y(t)$ and $X_C(t)$ are zero for $t < 0$. At $t = 0$ the system is turned on through a positive step change in $Y(t)$. Solving for $A(s)$ yields

$$A(s) \approx -\frac{\gamma_A s X_C(s)}{s^2 + \gamma_{A_0} s + \beta_A \gamma_M} + \frac{\beta_A \beta_M Y(s)}{s^2 + \gamma_{A_0} s + \beta_A \gamma_M} \quad \text{(Equation S7)}$$

To realize derivative control, we need to design parameter regimes for this motif where $A(s)$ is approximately proportional to $sX_C(s)$, the Laplace-domain representation of the time derivative of X_C.

To do so, we need to design the parameters of the derivative motif so that the denominator of the $X_C(s)$ bandpass transfer function, i.e. $-\frac{\gamma_A s}{s^2 + \gamma_{A_0} s + \beta_A \gamma_M} = -\frac{\gamma_A j\omega}{(j\omega)^2 + \gamma_{A_0} j\omega + \beta_A \gamma_M}$, becomes influential only at high frequencies. That is, at timescales faster than the fastest timescales of $X_C(j\omega)$. To begin, let's first define F to be $F = \int_0^{s_{max}} |X_C(s)| ds / \int_0^{\infty} |X_C(s)| ds$, where $s_{max} = j\omega_{max}$. Thus, $F = \int_0^{\omega_{max}} |X_C(j\omega)| j d\omega / \int_0^{\infty} |X_C(j\omega)| j d\omega$. Here ω_{max} is defined as the upper frequency of the integrand where the integral equals F. For this paper we choose $F = 0.99$. This is the frequency below which resides most of the frequency content of $X_C(j\omega)$. A conservative design choice is to suppose that the parameter values of the derivative motif are chosen such that $\beta_A \gamma_M \gg \left| s_{max}^2 + \gamma_{A_0} s_{max} \right|$. Likewise, the frequency domain equivalent would be $\beta_A \gamma_M \gg \left| -\omega_{max}^2 + \gamma_{A_0} j\omega_{max} \right|$. We denote these equivalent expressions as our design constraint. When the design constraint is satisfied, we obtain

$$A(s) \approx -\frac{\gamma_A s X_C(s)}{\beta_A \gamma_M} + \frac{\beta_A \beta_M Y(s)}{s^2 + \gamma_{A_0} s + \beta_A \gamma_M} \quad \text{(Equation S8)}$$

The expression $sX_C(s)$ in the Laplace domain corresponds to $\frac{dX_C}{dt}$ in the time domain. Transforming back to the time-domain yields the approximate expression

$$A \approx -\frac{\gamma_A}{\beta_A \gamma_M}\frac{dX_C}{dt} + h_Y * Y \quad \text{(Equation S9)}$$

where A is approximately equal to the negative time-derivative of X_C plus the impulse function between Y and A, i.e. h_Y, convolved with Y. Here h_Y is the inverse Laplace transform of the transfer function between $Y(s)$ and $A(s)$ in Equation S8. In this paper, Y is a

succession of step functions initially starting at $Y = 0$. Other than the sudden jump during a step change, Y will be at its current steady-state set-point value. During step changes in Y, where step changes contain higher frequencies that violate the design constraint, there will be brief fast transients in the time domain signal of A before accurate tracking of $\frac{dX_C}{dt}$ occurs. Thus, after this brief transient, $h_Y * Y = \beta_M Y/\gamma_M$. Neglecting this brief transient yields the tracking relationship Equation 16 in the main text. This implies that the signal of $\frac{d^2A(t)}{dt^2} + \gamma_{A_0}\frac{dA(t)}{dt}$ will, on average, be much smaller in magnitude than the signal of $\beta_A\gamma_M A(t)$ since $d^2A(t)/dt^2$ and $\gamma_{A_0} dA(t)/dt$ are not present in Equation 16. Figure S4 illustrates cases (different X_C inputs) when the design constraint is preserved, as well as cases when it is violated.

To be clear, the maximal frequency ω_{max} of X_C is that of the closed loop system, dependent on the parameters and the inputs. And it would change over the course of adjusting the control gains (β_I, β_P, β_D) while optimizing a design. This implies a very important question which is: what is the best way to iterate through designs of the PID controller when ω_{max} is changing for each design? Computationally, a quick and accurate way to iterate through designs, without needing ω_{max}, is to first design the control parameters (β_I, β_P, β_D) without the derivative motif. Instead, in the X_1 equation, we use an ideal derivative where we set $A = -\frac{\gamma_A}{\beta_A\gamma_M} dX_C/dt + \frac{\beta_M}{\gamma_M} Y$. This is easy to do since we calculate dX_C/dt in the ODE solvers during simulations. Once an acceptable design is obtained, we have ω_{max} over a whole range of set points, etc. We choose the highest one over the operational range of the controller. We then apply it to the frequency domain design constraint, $\left|(j\omega_{max})^2 + \gamma_{A_0} j\omega_{max}\right| \ll \beta_A\gamma_M$, where we can then easily solve for the derivative motif parameters in Equations 11 and 12 to ensure an accurate derivative tracker.

Analysis of Poles in Equation S7

The denominator in the transfer functions of the right side of Equation S7, i.e. $s^2 + \gamma_{A_0} s + \beta_A\gamma_M$, represents the multiplication of the poles of the system. The roots of the poles are solved using the quadratic formula which yields

$$s = -\frac{\gamma_{A_0}}{2} \pm \frac{\sqrt{\gamma_{A_0}^2 - 4\beta_A\gamma_M}}{2} \qquad \text{(Equation S10)}$$

This is a stable system since γ_{A_0}, β_A, and γ_M are all positive, therefore ensuring that the real parts of both poles are negative.

Below we analyze different relative values between γ_{A0} and $\beta_A\gamma_M$ to determine the timescales of the poles, relative to ω_{max}. To facilitate this, we present a more usable form of the design constraint $\left|-\omega_{max}^2 + \gamma_{A_0} j\omega_{max}\right| \ll \beta_A\gamma_M$ which can be written as

$$\left|-\omega_{max}^2 + \gamma_{A_0} j\omega_{max}\right| \leq \frac{\beta_A\gamma_M}{N} \qquad \text{(Equation S11)}$$

where $1/N$ is the acceptable relative error tolerance. In the paper, we use $N = 10$, a standard order of magnitude difference. Next without any loss of generality, we set $\gamma_{A_0} = \sqrt{\beta_A\gamma_M}/K$, where K is any positive real number. We define ω_{max^*} as the upper bound on ω_{max} that satisfies Equation S11 above. We would like to solve for ω_{max^*} as a function of the parameters, and compare that to the poles of the system. Squaring both sides of the design constraint yields

$$\omega_{max^*}^4 + \frac{\beta_A\gamma_M}{K^2}\omega_{max^*}^2 = \left(\frac{\beta_A\gamma_M}{N}\right)^2 \qquad \text{(Equation S12)}$$

Solving for $\omega_{max^*}^2$ give us

$$\omega_{max^*}^2 = -\frac{1}{2}\frac{\beta_A\gamma_M}{K^2} \pm \frac{\beta_A\gamma_M}{2}\sqrt{\frac{1}{K^4} + \frac{4}{N^2}} \qquad \text{(Equation S13)}$$

We take the positive solution to get

$$\omega_{max^*} = \sqrt{\frac{\beta_A\gamma_M}{2}\left[-\frac{1}{K^2} + \sqrt{\frac{1}{K^4} + \frac{4}{N^2}}\right]} \qquad \text{(Equation S14)}$$

Also, for this relationship between γ_{A_0} and $\beta_A\gamma_M$, the poles are given by:

$$s = -\frac{\sqrt{\beta_A\gamma_M}}{2K} \pm \frac{\sqrt{\beta_A\gamma_M\left(\frac{1}{K^2} - 4\right)}}{2} \qquad \text{(Equation S15)}$$

It is then clear that if $K > 1/2$, then the poles are complex, and conversely if $K < 1/2$, then the poles are real. Also, since $\frac{4}{N^2} \ll 1$, then for cases when $K \leq 1$, the $\sqrt{\frac{1}{K^4} + \frac{4}{N^2}}$ term from Equation S14 above can be approximated to a first order as $\frac{1}{K^2} + \frac{2K^2}{N^2}$ which we will use (see **Derivation 1** below). We now discuss a few parameter regimes:

- **Case 1:** $K = 1$, that is $\gamma_{A_0}^2 = \beta_A\gamma_M$. The poles of the system are complex, with the same real part being $-\sqrt{\beta_A\gamma_M}/2$. In this case, it can be shown that $\sqrt{1 + \frac{4}{N^2}}$ can be approximated as $1 + \frac{2}{N^2}$ (see **Derivation 1** below that shows an approximation that is valid for

all K less or equal than one). Plugging this into Equation S14 yields $\omega_{max^*} \approx \sqrt{\beta_A \gamma_M}/N$. Given that $\gamma_{A_0}/2 = \sqrt{\beta_A \gamma_M}/2$ then the real part of the poles is about N/2 times faster than ω_{max^*}. For this case, the magnitude of the real part of the pole, $\gamma_{A_0}/2$ is large relative to ω_{max^*}. In addition, this also implies that $j\gamma_{A_0}\omega_{max^*}$ is the dominant term on the left side of the design constraint in Equation S11 above, and the error incurred is a phase error.

- **Case 2:** $K \ll 1$**.** When $K \ll 1$, then $\gamma_{A_0}^2 \gg 4\beta_A \gamma_M$, and hence the poles are real. The largest one has a magnitude of approximately $\frac{\sqrt{\beta_A \gamma_M}}{K} - K\sqrt{\beta_A \gamma_M}$. The smallest one has a magnitude of approximately $K\sqrt{\beta_A \gamma_M}$ (see **Derivation 2** below for derivation of the poles). Since $K \ll 1$, we can approximate $\sqrt{\frac{1}{K^4} + \frac{4}{N^2}}$ with $\frac{1}{K^2} + \frac{2K^2}{N^2}$. Thus, $\omega_{max^*} \approx \sqrt{\beta_A \gamma_M}\, K/N$. Hence, ω_{max^*} is a factor of N smaller than the smallest pole. Even more stringent than case 1. Again, the magnitude of both poles is large relative to ω_{max^*}. As in Case 1, $j\gamma_{A_0}\omega_{max^*}$ is the dominant term on the left side of the design constraint in Equation S11 above.
- **Case 3:** $K \gg 1$**.** We will start with the specific case of $K = 10$, $N = 10$. Plugging these values in Equation S14 yields $\omega_{max^*} \approx \sqrt{\beta_A \gamma_M}/3.2$. In this case, the poles are complex, with a real part whose magnitude is equal to $\sqrt{\beta_A \gamma_M}/20$. Therefore, ω_{max^*} is about 6 times larger than the real part of the poles. However, the imaginary part of the poles have a magnitude of $\approx \sqrt{\beta_A \gamma_M}$ and are therefore larger than ω_{max^*} (about 3 times faster). In this case the dominant approximation error is $-\omega_{max}^2$, an amplitude error. Finally, for $K \geq N$, the $\gamma_{A_0} j\omega_{max^*}$ term in Equation S11 above is negligible, yielding the general expression $\omega_{max^*} \approx \sqrt{\beta_A \gamma_M}/\sqrt{N}$ and the same analysis applies.

We confirmed these insights using simulations for all three cases (case 1: $K = 1$, $N = 10$, case 2: $K = 0.1$, $N = 10$, and case 3: $K = 10$, $N = 10$). For all cases the output of the derivative motif $A(t)$ tracks $-dX_C(t)/dt$ very well for inputs whose frequency content is under ω_{max^*} (Figure S4, time-domain plots), and accurate tracking is lost above it. Note that these are all deterministic solutions. However if one is considering noise within the system, then positioning the design along the scenario of case 1 will be the best since its transfer function $H(j\omega)$ will amplify the least amount of noise above ω_{max^*} (Figure S4, frequency domain plots). Case 2 will be the worst while case 3 will be somewhere in between due to its sharp peak.

In a nutshell, these results indicate that either the real part of the poles need to be faster than ω_{max^*}, and/or the complex part needs to be faster than ω_{max^*} for accurate derivative tracking at $N = 10$.

Derivation 1

Consider a first order Taylor series expansion of $\sqrt{C+x}$ where $C \geq 1$ and $x \ll 1$. Here $\sqrt{C+x} \approx \sqrt{C} + \frac{x}{2\sqrt{C}}$. When $C = \frac{1}{K^4} \geq 1$ and $x = \frac{4}{N^2} \ll 1$, then have $\sqrt{\frac{1}{K^4} + \frac{4}{N^2}} \approx \frac{1}{K^2} + \frac{2K^2}{N^2}$. This is satisfied when $K \leq 1$. For this paper $\frac{4}{N^2} \ll 1$ since N will always be 10 or greater.

Derivation 2

For approximating the poles in case 2 ($K \ll 1$), we can apply the same Taylor series approach from **Derivation 1**. From Equations S10 and S15, the $\frac{\sqrt{\gamma_{A_0}^2 - 4\beta_A \gamma_M}}{2} = \frac{\sqrt{\beta_A \gamma_M}}{2K}\sqrt{1 - 4K^2}$ term can be approximated as $\frac{\sqrt{\beta_A \gamma_M}}{2K}[1 - 2K^2]$ where $C = 1$ and $x = -4K^2$. Therefore Equation S15 can be approximated as

$$s = -\frac{\sqrt{\beta_A \gamma_M}}{2K} \pm \frac{\sqrt{\beta_A \gamma_M}}{2K}\left[1 - 2K^2\right] \qquad \text{(Equation S16)}$$

where one can see the the largest pole is $-\frac{\sqrt{\beta_A \gamma_M}}{K} + K\sqrt{\beta_A \gamma_M}$ and the smallest pole is $-K\sqrt{\beta_A \gamma_M}$.

An Alternative Derivative Motif

We present an alternative derivative motif that allows for an approximate computation of $\mu\frac{dy}{dt} - \theta\frac{dX_C}{dt}$. We use a proportional-like input function, $(\theta X_C)/(\mu Y + \theta X_C)$, whose time-derivative will be measured by the motif to get

$$\frac{dA}{dt} = \beta_A M - \frac{4Y_0}{\theta}\gamma_A \frac{\theta X_C}{\mu Y + \theta X_C}\frac{A}{K_A + A} - \gamma_{A_0} A \qquad \text{(Equation S17a)}$$

$$\frac{dM}{dt} = \beta_M Y_0 - \gamma_M A \frac{M}{K_M + M} \qquad \text{(Equation S17b)}$$

where Y_0 is a constant ($Y_0 = 300$ nM for simulations). When the active degradation is occurring at saturation and the design constraint $\beta_A \gamma_M \gg \left|s_{max}^2 + \gamma_{A_0} s_{max}\right|$ holds (see STAR Methods "Realizing the derivative control term"), the system in the Laplace domain simplifies to

$$A(s) \approx -\frac{\frac{4Y_0}{\theta}\gamma_A s \frac{\theta X_C}{\mu Y + \theta X_C}}{\beta_A \gamma_M} + \frac{\beta_M Y_0}{\gamma_M} \qquad \text{(Equation S18)}$$

whose time domain expression becomes

$$A(t) \approx -\frac{\frac{4Y_0}{\theta}\gamma_A \frac{d\left[\frac{\theta X_C(t)}{\mu Y(t)+\theta X_C(t)}\right]}{dt}}{\beta_A \gamma_M} + \frac{\beta_M Y_0}{\gamma_M} \quad \text{(Equation S19)}$$

An altered X_1 equation must be used where now $D_t(X_C, Y) = (\beta_D Y / Y_0)A$, i.e.

$$\frac{dX_1}{dt} = \beta_I Z_1 + f_P(X_C, Y) + \frac{\beta_D Y}{Y_0} A - \gamma_1 X_1 \quad \text{(Equation S20)}$$

This alternative D motif is discussed in Section ''PID benefits depend on the process to be controlled and PID gains need to be tuned'' showing it provides better set-point tracking dynamics upon step-changes in the input Y. In STAR Methods ''Linearized analysis of the alternative derivative motif'', we linearize Equation S19 to show how it provides an approximate $\mu\frac{dy}{dt} - \theta\frac{dX_C}{dt}$.

Experimentally, the realization of this new input to the derivative motif can be achieved using the same basic approach we propose to realize $f_P(X_C,Y)$ in STAR Methods ''Experimental realization of proportional control function''.

The Control Circuit Equations Linearized about a Set-Point

Our goal here is to linearize the biochemical PID controller and process to relate it to the textbook linear PID case discussed in Section ''Linear perturbation analysis of nonlinear PID control design provides analytical support for the design''. We will derive the Laplace-domain transfer function between μy and θx_c for our linearized PID biochemical controller.

As a means of evaluating perturbations about a set-point, we linearized Equations 6, 7, and 8 and the simplified derivative motif equation Equation 16 around some steady state $Y_{ss}, X_{C_{ss}}, X_{1_{ss}}, Z_{1_{ss}}, Z_{2_{ss}}, A_{ss}$. The steady-state values are computed as:

$$0 = \mu Y_{ss} - \eta Z_{1_{ss}} Z_{2_{ss}} \quad \text{(Equation S21a)}$$

$$0 = \theta X_{C_{ss}} - \eta Z_{1_{ss}} Z_{2_{ss}} \quad \text{(Equation S21b)}$$

$$0 = \beta_I Z_{1_{ss}} + \beta_P Y_{ss} \frac{\alpha_P Y_{ss}}{\alpha_P Y_{ss} + X_{C_{ss}}} + \beta_D A_{ss} - \gamma_1 X_{1_{ss}} \quad \text{(Equation S21c)}$$

$$0 = \beta_M Y_{ss} - \gamma_M A_{ss} \quad \text{(Equation S21d)}$$

The linearized time-dependent perturbed system is

$$\frac{dz_1}{dt} = \mu y - \eta Z_{2_{ss}} z_1 - \eta Z_{1_{ss}} z_2 \quad \text{(Equation S22a)}$$

$$\frac{dz_2}{dt} = \theta x_C - \eta Z_{2_{ss}} z_1 - \eta Z_{1_{ss}} z_2 \quad \text{(Equation S22b)}$$

$$\frac{dx_1}{dt} = \beta_I z_1 + \beta_P \left[\frac{2\alpha_P Y_{ss}}{\alpha_P Y_{ss} + X_{C_{ss}}} - \left(\frac{\alpha_P Y_{ss}}{\alpha_P Y_{ss} + X_{C_{ss}}}\right)^2\right] y - \beta_P Y_{ss} \frac{\alpha_P Y_{ss}}{(\alpha_P Y_{ss} + X_{C_{ss}})^2} x_C + \beta_D a - \gamma_1 x_1 \quad \text{(Equation S22c)}$$

$$a = -\frac{\gamma_A}{\beta_A \gamma_M}\frac{dx_C}{dt} + \frac{\beta_M}{\gamma_M} y \quad \text{(Equation S22d)}$$

The equations were derived by computing the Jacobian matrix of the nonlinear system and evaluating at steady state (Strogatz, 2014). The approximate solution is locally equal to the steady-state solution plus the perturbed solution, for example, the time-dependent solution for X_1 would be $X_1(t) = X_{1_{ss}} + x_1(t)$. Likewise, the input Y would be $Y(t) = Y_{ss} + y(t)$. Transforming this set of linear equations into the Laplace domain, we obtain

$$sz_1(s) = \mu y(s) - \eta Z_{2_{ss}} z_1(s) - \eta Z_{1_{ss}} z_2(s) \quad \text{(Equation S23a)}$$

$$sz_2(s) = \theta x_C(s) - \eta Z_{2_{ss}} z_1(s) - \eta Z_{1_{ss}} z_2(s) \quad \text{(Equation S23b)}$$

$$sx_1(s) = \beta_I z_1(s) + \beta_P \left[\frac{2\alpha_P Y_{ss}}{\alpha_P Y_{ss} + X_{C_{ss}}} - \left(\frac{\alpha_P Y_{ss}}{\alpha_P Y_{ss} + X_{C_{ss}}} \right)^2 \right] y(s) - \beta_P Y_{ss} \frac{\alpha_P Y_{ss}}{(\alpha_P Y_{ss} + X_{C_{ss}})^2} x_C(s) + \beta_D a(s) - \gamma_1 x_1(s) \quad \text{(Equation S23c)}$$

$$a(s) = -\frac{\gamma_A}{\beta_A \gamma_M} s x_C(s) + \frac{\beta_M}{\gamma_M} y(s) \quad \text{(Equation S23d)}$$

To facilitate notation, we designate $k_P\theta = \frac{\beta_P Y_{ss}}{\theta} \frac{\alpha_P Y_{ss}}{(\alpha_P Y_{ss} + X_{C_{ss}})^2} \theta = \frac{\beta_P}{\alpha_P \theta} \frac{(\alpha_P)^2}{(\alpha_P + \mu/\theta)^2} \theta$. When $\alpha_P \approx \mu/\theta$, the proportional function provides both sensitivity and dynamic range in both directions of X_C (see Section "Design of a proportional control term" for discussion). Likewise, when $\alpha_P \approx \mu/\theta$, $k_P\theta = \frac{\beta_P}{4\mu}\theta$. For the rest of the derivation we assume $\alpha_P \approx \mu/\theta$. We also designate $k_D\theta = \beta_D \frac{\gamma_A}{\beta_A \gamma_M}$ (see Section "Design of a derivative control term"). Substituting these constants and the relationship for $a(s)$ in Equation S23D into Equation S23C the equation becomes

$$sx_1(s) = \beta_I z_1(s) + \left[3k_P + \frac{\theta \beta_A \beta_M}{\gamma_A \mu} k_D \right] \mu y(s) - [k_P + s k_D] \theta x_C(s) - \gamma_1 x_1(s) \quad \text{(Equation S24)}$$

Let $f(s)$ be the transfer function of the linearized process to be controlled by $x_1(s)$. Thus, $x_C(s) = f(s)x_1(s)$. Using this relationship into Equation S24, we obtain after rearrangement

$$\frac{s + \gamma_1}{f(s)} x_C(s) = \beta_I z_1(s) + \left[3k_P + \frac{\theta \beta_A \beta_M}{\gamma_A \mu} k_D \right] \mu y(s) - [k_P + s k_D] \theta x_C(s) \quad \text{(Equation S25)}$$

We then use Equations S23A and S23B to derive an expression of $z_1(s)$ in terms of $x_C(s)$ and $y(s)$, and use this expression in the equation above to generate:

$$\frac{s + \gamma_1}{f(s)} x_C(s) = \frac{\beta_I (s + \eta Z_{1_{ss}}) \mu y(s) - \beta_I \eta Z_{1_{ss}} \theta x_C(s)}{s^2 + (\eta Z_{1_{ss}} + \eta Z_{2_{ss}}) s} + \left[3k_P + \frac{\theta \beta_A \beta_M}{\gamma_A \mu} k_D \right] \mu y(s) - [k_P + s k_D] \theta x_C(s) \quad \text{(Equation S26)}$$

Letting $\Phi(s) = \frac{f(s)}{s + \gamma_1}$, we can rearrange Equation S26 to obtain the Laplace-domain relationship between $x_C(s)$ and $y(s)$ of Equation 19 given by:

$$x_C(s) = \frac{\left[\beta_I \frac{s + \eta Z_{1_{ss}}}{s + \eta Z_{1_{ss}} + \eta Z_{2_{ss}}} + 3sk_P + \frac{\theta \beta_A \beta_M}{\gamma_A \mu} s k_D \right] \Phi(s)}{s + \theta \left[\beta_I \frac{\eta Z_{1_{ss}}}{s + \eta Z_{1_{ss}} + \eta Z_{2_{ss}}} + sk_P + s^2 k_D \right] \Phi(s)} \mu y(s) \quad \text{(Equation S27)}$$

At steady state, i.e. $s = 0$, it is easy to see that $\mu y(s = 0) = \theta x_C(s = 0)$, consistent with the full nonlinear system. While k_D and k_P are constants that are dependent on parameters, the integral gain terms in the numerator and denominator of Equation S27 are a function of the Laplace-domain variable s. However, if the upper-bound of the frequency content of $x_C(s)$, i.e. ω_{max} is known, where $s_{max} = j\omega_{max}$, then the parameter η of the antithetic integral controller can be designed such that $|s_{max}| = |j\omega_{max}| \ll \eta Z_{1_{ss}}$. The mathematical definition for ω_{max} is the same one used in STAR Methods "Realizing the derivative control term". In the case where $|s_{max}| = |j\omega_{max}| \ll \eta Z_{1_{ss}}$, the integral terms in the numerator and denominator can be approximated as $k_I = \frac{\beta_I Z_{1_{ss}}}{Z_{1_{ss}} + Z_{2_{ss}}}$. This approximation conforms the numerator and denominator terms that are associated with integral control to the traditional PID expression. Making this approximation in Equation 19 and letting the integral control weight $k_I = \frac{\beta_I Z_{1_{ss}}}{Z_{1_{ss}} + Z_{2_{ss}}}$ yields Equation 20 in the main text. For the processes we use in this paper, the highest calculated ω_{max} was approximately 0.25 rad min^{-1}. For our lowest input values Y = 60 nM, $\eta Z_{1_{ss}} \approx 2.5$ rad min^{-1}, about an order of magnitude larger than ω_{max}. Thus, even for this worst case, $|s_{max}| = |j\omega_{max}| \ll \eta Z_{1_{ss}}$. For Y = 300 nM, $\eta Z_{1_{ss}} \approx 12$ rad min^{-1}. In general for larger Y, $\eta Z_{1_{ss}}$ scales approximately with Y.

While the analyses above derive linearization and proportional gains for the final form of the proportional control, similar treatment can be extended to the other proportional control functions that are analyzed and compared. For the proportional control function $\beta_P \frac{(\mu K_C/\theta)}{(\mu K_C/\theta) + X_C}$, we get $k_P\theta = \beta_P \frac{(\mu K_C/\theta)}{((\mu K_C/\theta) + X_{C_{ss}})^2} = \beta_P \frac{(\mu K_C/\theta)}{((\mu K_C/\theta) + \mu Y_{ss}/\theta)^2}$. And for the proportional control function $\beta_P \frac{\alpha_P Y}{\alpha_P Y + X_C}$, we get $k_P\theta = \beta_P \frac{\alpha_P Y_{ss}}{(\alpha_P Y_{ss} + X_{C_{ss}})^2} = \frac{\beta_P}{\alpha_P \theta Y_{ss}} \frac{(\alpha_P)^2}{(\alpha_P + \mu/\theta)^2} \theta$ which becomes $k_P\theta = \frac{\beta_P}{4\alpha_P \theta Y_{ss}} \theta$ for $\alpha_P \approx \mu/\theta$.

Finally, to assess the accuracy of the linearization for the parameter values used, we simulated the linearized system and compared it to the full nonlinear system (Figures 4 and S7). In addition, we also simulated a traditional PID controller where we coupled the process equation, Equation 5, with an X_1 equation that uses the traditional error terms

$$\frac{dx_1}{dt} = k_I \int_0^t [\mu y(t') - \theta x_C(t')] dt' + k_P [\mu y - \theta x_C] + k_D \left[\mu \frac{dy}{dt} - \theta \frac{dx_C}{dt} \right] - \gamma_1 x_1 \quad \text{(Equation S28)}$$

The $\frac{dy}{dt}$ term cannot be infinite for ODE solvers, so we simulate the step function with a finite transition time of about 2 min, still much faster than the time-scales of rest of the system which is all that matters. We can decrease the transition time further without any effect in the solution. Equation S28 can be used to compare the linearized biochemical controller to the traditional one, especially scrutinizing the approximation made for k_I. Specifically, the transfer function for the traditional PID controller using Equation S28 for a step change $\Delta\beta_C$ in β_C is:

$$x_C(s) = \frac{\frac{s\Delta\beta_C X_{1ss}}{s+\gamma_C}}{s+\theta\left[\beta_I\frac{\eta Z_{1_{ss}}}{\eta Z_{1_{ss}}+\eta Z_{2_{ss}}}+sk_P+s^2k_D\right]\Phi(s)} \quad \text{(Equation S29)}$$

That of the biochemical controller is:

$$x_C(s) = \frac{\frac{s\Delta\beta_C X_{1ss}}{s+\gamma_C}}{s+\theta\left[\beta_I\frac{\eta Z_{1_{ss}}}{s+\eta Z_{1_{ss}}+\eta Z_{2_{ss}}}+sk_P+s^2k_D\right]\Phi(s)} \quad \text{(Equation S30)}$$

Comparing both, once can see that the integral control gains become more similar to each other as $\eta Z_{1_{ss}}$ increases, which occurs when Y increases. For our examples in this paper, $Y_{ss} = 600$ nM is a large enough value (Figure S7C) such that the linearized biochemical PID and the traditional linear PID have a very similar response and hence the linearized biochemical PID is exhibiting a constant k_I in this regime.

For the system simulated to generate Figures 4A and S7A, the traditional linear PID agree well with the linearized biochemical PID. For the case of the process with delay only (Section "PID benefits depend on the process to be controlled and PID gains need to be tuned"), we simulated the linearized version and the traditional linear controller for case 1 from Figure 5A. The full system and the linearized version agree well while the traditional linear controller has a much slower convergence rate (Figure S7D). Given that there is no derivative term in this case, the only source for the differences is the $3k_Py$ (linearized version) versus k_Py (traditional). We simulated the linearized biochemical controller but dividing the $3k_Py$ by 3, which resulted in identical results for the traditional and biochemical controller (Figure S7D, linearized (k_Py)). Interestingly the $3k_Py$ term in the biochemical controller helps accelerate convergence relative to the traditional case.

Linearized Analysis of the Alternative Derivative Motif

Here we determine the approximate transfer function for the PID controller when the alternative D motif (STAR Methods "An alternative derivative motif") is used. Linearizing Equations S19 and S20 yields

$$a(t) \approx -\frac{\frac{4Y_0}{\theta}\gamma_A\left[\frac{\mu Y_{ss}}{(\mu Y_{ss}+\theta X_{C_{ss}})^2}\theta\frac{dx_C}{dt}-\frac{\theta X_{C_{ss}}}{(\mu Y_{ss}+\theta X_{C_{ss}})^2}\mu\frac{dy}{dt}\right]}{\beta_A\gamma_M} \quad \text{(Equation S31)}$$

and

$$\begin{aligned}\frac{dx_1}{dt} &= \beta_I z_1 + 3\frac{\beta_P}{4\mu}\mu y - \frac{\beta_P}{4\mu}\theta x_C + \frac{\beta_D A_{ss}}{Y_0}y + \frac{\beta_D Y_{ss}}{Y_0}a - \gamma_1 x_1 \\ &= \beta_I z_1 + 3\frac{\beta_P}{4\mu}\mu y - \frac{\beta_P}{4\mu}\theta x_C + \frac{\beta_D\beta_M}{\gamma_M}y + \frac{\beta_D\gamma_A}{\mu\theta\beta_A\gamma_A}\left[\mu\frac{dy}{dt}-\theta\frac{dx_C}{dt}\right] - \gamma_1 x_1\end{aligned} \quad \text{(Equation S32)}$$

We then set $k_D = \frac{\beta_D\gamma_A}{\mu\theta\beta_A\gamma_A}$ and following the same procedure as we did above for deriving the transfer function for the biochemical PID with the original D motif (Equation 20), we get

$$x_C(s) \approx \frac{\left[k_I + 3sk_P + \frac{\beta_D\beta_M}{\mu\gamma_M}s + s^2k_D\right]\Phi(s)}{s+\theta[k_I+sk_P+s^2k_D]\Phi(s)}\mu y(s) \quad \text{(Equation S33)}$$

It has the same basic form as Equation 20, but with the addition of a k_Ds^2 term in the numerator. As discussed in Section "PID benefits depend on the process to be controlled and PID gains need to be tuned", this extra term can improve set-point tracking dynamics due to step-changes in μy.

Linearized Analysis of the integral Controller from Equation 25

We can carry the same linearization analyses as above to Equation 25, assuming that degradation occurs at saturation ($K_Z \ll Z$). This yields

$$\frac{dz}{dt} \approx \beta_Z \left[\frac{2\alpha_P Y_{ss}}{\alpha_P Y_{ss} + X_{C_{ss}}} - \left(\frac{\alpha_P Y_{ss}}{\alpha_P Y_{ss} + X_{C_{ss}}} \right)^2 \right] y - \beta_Z Y_{ss} \frac{\alpha_P Y_{ss}}{(\alpha_P Y_{ss} + X_{C_{ss}})^2} x_C - \gamma_Z y \quad \text{(Equation S34)}$$

whose Laplace-domain equation when $\alpha_P = \mu/\theta$ and $\gamma_Z = \beta_Z/2$ and $\theta X_{C_{ss}} = \mu Y_{ss}$ is

$$\begin{aligned} sz(s) &\approx 3\frac{\beta_Z}{4\mu}\mu y - \frac{\beta_Z}{4\mu}\theta x_C - \frac{\beta_Z}{2\mu}\mu y \\ &\approx \frac{\beta_Z}{4\mu}[\mu y - \theta x_C] \end{aligned} \quad \text{(Equation S35)}$$

We can then take Equation S25 which relates the $x_C(s)$ to $y(s)$ for the antithetic PID and replace the antithetic integral control term $\beta_I z_1(s)$ with the new integral control term $\beta_I^* z(s)$ to get

$$\begin{aligned} \frac{s+\gamma_1}{f(s)} x_C(s) &= \beta_I^* z(s) + \left[3k_P + \frac{\theta\beta_A\beta_M}{\gamma_A\mu} k_D \right] \mu y(s) - [k_P + sk_D]\theta x_C(s) \\ &= \left[\beta_I^* \frac{\beta_Z}{s4\mu} + 3k_P + \frac{\theta\beta_A\beta_M}{\gamma_A\mu} k_D \right] \mu y(s) - \left[\beta_I^* \frac{\beta_Z}{s4\mu} + k_P + sk_D \right] \theta x_C(s) \end{aligned} \quad \text{(Equation S36)}$$

where we set $k_I = \beta_I^* \frac{\beta_Z}{4\mu}$ to get the transfer function

$$x_C(s) = \frac{\left[k_I + 3sk_P + \frac{\theta\beta_A\beta_M}{\gamma_A\mu} sk_D \right] \Phi(s)}{s + \theta[k_I + sk_P + s^2 k_D]\Phi(s)} \mu y(s) \quad \text{(Equation S37)}$$

Which has exactly the same form as the transfer function for the antithetic system, Equation 20. The only difference being $k_I = \beta_I^* \frac{\beta_Z}{4\mu}$ for the new PID while $k_I = \frac{\beta_I Z_{1_{ss}}}{(Z_{1_{ss}} + Z_{2_{ss}})}$ for the antithetic PID, a function of the steady-state Z_1 and Z_2 values. When simulating the new PID in Section "Constructing a PID controller with a different integral controller architecture" for Figures 7A and 7B, we enforce that $k_I = 0.058 = \beta_I^* \frac{\beta_Z}{4\mu}$, where we set $\beta_I^* = 0.058 \frac{4\mu}{\beta_Z}$ to obtain approximately the same k_I value for both strategies for fair comparison.

Applicability of Antithetic PID Controller to Arbitrary Processes

For the antithetic PID controller to be able to control a given process, it must be tuned so that it provides both zero stead-state tracking error, i.e. $\mu Y = \theta X_{C_{ss}}$, and stability. In the original work on the antithetic integral controller (Briat et al., 2016), the authors find that for zero steady-state tracking error over all values of the set-point Y, the integral controller variable Z_1 must positively regulate X_C. With the addition of P and D terms, we show that Z_1 still positively regulates X_C (see STAR Methods "Z_1 positively regulates X_C in the presence of P and D terms" for proof). Therefore any process that exhibits this property, however complicated, will yield zero steady-state error, as long as the integral controller is working. For the antithetic integral controller to work, Z_1 and Z_2 must reach steady state and be non-zero. In STAR Methods "Bounds on antithetic integral control with P and D terms", we discuss the conditions for this to hold. However, zero steady-state error does not imply that the system is stable, the second requirement for the PID to control a given process. A general stability analysis for a full nonlinear system is difficult. However, through the linearized analysis for a given PID controller and process, standard techniques can be used to check whether the system is locally stable.

Z_1 Positively Regulates X_C in the Presence of P and D Terms

Given that X_1 positively regulates X_C, we will show that even in the presence of P and D control terms, Z_1 positively regulates X_C. To begin, we assume that for the open loop process, the steady-state X_C is a monotonically increasing and non-saturating function of steady-state X_1. What this implies is that $\frac{dX_C}{dX_1} > 0$. We denote the steady-state relationship of X_C and X_1 as $X_C(X_1)$. For the simple process used as an example in this paper, when $\frac{dX_C}{dt} = \beta_C X_1 - \gamma_C X_C$, then $X_C(X_1) = \frac{\beta_C}{\gamma_C} X_1$. Note here that in order to minimize cumbersome notation, we will just use X_1 to denote the steady state of X_1 and so on. For the closed-loop system with P and D control terms, the steady-state for X_1 can by computed by setting $\frac{dX_1}{dt} = 0$ in Equation 8 in the main text, resulting in the steady-state X_1 equation:

$$\beta_I Z_1 + \beta_P Y \frac{\mu Y}{\mu Y + \theta X_C} + \beta_D \frac{\beta_M}{\gamma_M} Y = \gamma_1 X_1 \quad \text{(Equation S38)}$$

Therefore, X_1 is a function of Y and Z_1 (explicitly, and also through $X_C(X_1)$). We will therefore, denote it by $X_1(Z_1,Y)$. If we set $\beta_P = 0$ (I and ID cases, no proportional control), then for a given Y, X_1 is a monotonically increasing function of Z_1, and since $\frac{dX_C}{dX_1} > 0$ then X_C is also an increasing function of Z_1. Thus, Z_1 positively regulates X_C, given Y.

Now, if we set $\beta_P > 0$ (PI and PID cases), then we need to prove that $X_1(Z_1,Y)$ is a monotonically increasing function of Z_1, given Y (implying as above that $X_C(X_1(Z_1,Y))$ is a monotonically increasing function of Z_1 for a given Y). To begin we will differentiate Equation S38 with respect to Z_1 to get

$$\beta_I - \frac{dX_1}{dZ_1}\frac{dX_C}{dX_1}\beta_P Y \frac{\mu Y}{(\mu Y + \theta X_C)^2} = \gamma_1 \frac{dX_1}{dZ_1} \quad \text{(Equation S39)}$$

which we can rearrange and solve for dX_1/dZ_1 to get

$$\frac{dX_1}{dZ_1} = \frac{\beta_I}{\frac{dX_C}{dX_1}\beta_P Y \frac{\mu Y}{(\mu Y + \theta X_C)^2} + \gamma_1} \quad \text{(Equation S40)}$$

Where it is easy to see that $dX_1/dZ_1 > 0$, thus proving that $X_1(Z_1, Y)$ is a monotonically increasing function of Z_1, given Y.

For this to hold, we must now also prove that solution of X_1 is unique for a given Z_1 and Y. This can be seen by looking at Equation S38 above. For a given Z_1 and Y, the left side is a monotonically decreasing function of X_1 (through $X_C(X_1)$) beginning at $\beta_I Z_1 + \beta_P Y + \beta_D \frac{\beta_M}{\gamma_M} Y$ and asymptotically decreasing to $\beta_I Z_1 + \beta_D \frac{\beta_M}{\gamma_M} Y$. The right side, $\gamma_1 X_1$, will always cross this curve at a unique value (Figure S8A). Thus, $X_1(Z_1, Y)$ is a unique monotonically increasing function of Z_1. And as above it follows that $X_C(X_1(Z_1, Y))$ is a monotonically increasing function of Z_1, given Y. Thus, Z_1 positively regulates X_C, given Y.

Bounds on Antithetic Integral Control with P and D Terms

The steady-state X_1 equation is

$$\beta_I Z_1 + \beta_P Y \frac{\mu Y}{\mu Y + \theta X_C} + \beta_D \frac{\beta_m}{\gamma_M} Y = \gamma_1 X_1 = \frac{\gamma_1}{G} X_C \quad \text{(Equation S41)}$$

Where G is the steady-state gain between X_1 and X_C through the process, i.e. $X_C = GX_1$, a linear relationship for this exercise. For the antithetic integral controller to work, Z_1 and Z_2 must be non-zero and reach steady state. When this holds, in the presence of P and D terms, we get the following relationship

$$\beta_I Z_1 + \frac{\beta_P}{2} Y + \beta_D \frac{\beta_m}{\gamma_M} Y = \frac{\gamma_1 \mu}{G\theta} Y \quad \text{(Equation S42)}$$

The important point is that as one increases β_P and β_D, the P and D gains, Z_1 decreases. The integral controller breaks when $Z_1 = 0$, after which this relation no longer holds and Z_2 grows over time, as we show in Figures S1C–S1E. Equation S42 implies that as long as

$$\frac{\beta_P}{2} + \beta_D \frac{\beta_m}{\gamma_M} < \frac{\gamma_1 \mu}{G\theta} \quad \text{(Equation S43)}$$

the integral controller is working and there will be zero steady-state error. However, this does not mean that the system is stable, the second requirement for the PID to control the process.

The examples in Figures S1C–S1E satisfy Equation S43 for $t \leq 0$ where β_P and β_D are zero. At $t = 0$, the parameters are changed so that Equation S43 does not hold. Here integral control is broken where we observe in Figures S1C–S1E that $\frac{dZ_1}{dt} \to 0$ and $Z_1 \to 0$ but $\frac{dZ_2}{dt} = r$, where r is observed to be a positive constant. For these cases, since $\frac{dZ_1}{dt} \to 0$, Equation 6 becomes $\mu Y = \eta Z_1 Z_2$. Substituting this result into Equation 7 yields

$$\frac{dZ_2}{dt} = \theta X_C - \mu Y = r \quad \text{(Equation S44)}$$

Note that X_C reaches a steady-state value, uncoupled from the integral control, and thus r must be a constant given that Y is a constant. Thus, $\theta X_C = \mu Y + r$ and $Z_2 = \mu Y / Z_1$, where $Z_1 \to 0$ as $t \to \infty$.

For the PI numerical example in Figure S1C, we measured $dZ_2/dt = r = \theta X_C - \mu Y$ to be $r \approx 91$ nM/min. For the ID numerical example in Figure S1D, we measured $r \approx 75$ nM/min. And for the PID numerical example in Figure S1E, we measured $r \approx 85$ nM/min. For these cases, we also numerically solved for X_C in Equation S41 above when integral control is broken ($Z_1 \to 0$). This enabled us to calculate r which was in excellent agreement with the simulation results. In the numerical examples we also observed that $\mu Y = \eta Z_1 Z_2$, as predicted by the theory. Although as $Z_1 \to 0$ with increasing time, we observe increasing numerical roundoff error in the $\eta Z_1 Z_2$ term as one would expect.

We also examined the parameter search results in Figure S5B to look at the boundary at which the system loses perfect adaptation (edge of blue and white regions). In other words, the boundary is where Equation S43 becomes violated as one moves into the white region. For this example, $G = 1.5$. For the PI case when we solve Equation S43 for β_P at this critical value we get $\beta_P = 0.44$. And for the ID case we get $\beta_D = 0.79$. This agrees well with the plots in Figure S5B. One can see that the boundaries are independent (within the tolerance of the parameter sampling) of β_I as predicted by the theory.

Steady-State Analysis of Integral Controller from Equation 25

For the integral controller presented in Section "Constructing a PID controller with a different integral controller architecture", we go through the general proof for a unique solution to Equation 25 at steady state. We will also discuss requirements for an operational integral controller. To begin, we assume that for the open loop process, the steady-state X_C is a monotonically increasing and non-saturating function of steady-state X_1. What this implies is that $\frac{dX_C}{dX_1}>0$. We denote the steady-state relationship of X_C and X_1 as $X_C(X_1)$. For example, for the simple process used as an example in this paper, when $\frac{dX_C}{dt} = \beta_C X_1 - \gamma_C X_C$, then $X_C(X_1) = \frac{\beta_C}{\gamma_C} X_1$. Note here that in order to minimize cumbersome notation, we will just use X_1 to denote the steady state of X_1 and so on. For the closed-loop system with P and D control terms, the steady state for X_1 can by computed by setting $\frac{dX_1}{dt} = 0$ in Equation 28 in the main text, resulting in the steady-state X_1 equation:

$$\beta_I^* Z + \beta_P Y \frac{\mu Y}{\mu Y + \theta X_C} + \beta_D \frac{\beta_M}{\gamma_M} Y = \gamma_1 X_1 \qquad \text{(Equation S45)}$$

Therefore, X_1 is a function of Y and Z (explicitly, and also through $X_C(X_1)$). We will therefore, denote it by $X_1(Z,Y)$. At the same time, Equation 25 generates the relationship between Z and X_C at steady state:

$$\frac{\beta_Z}{\gamma_Z} \frac{\mu Y}{\mu Y + \theta X_C(X_1(Z,Y))} = \frac{Z}{Z + K_Z} \qquad \text{(Equation S46)}$$

The steady state for Z is the intersection of the function $\frac{Z}{Z+K_Z}$ and $\frac{\beta_Z}{\gamma_Z} \frac{\mu Y}{\mu Y + \theta X_C(X_1(Z,Y))}$ as they are plotted as a function of Z. The function $\frac{Z}{Z+K_Z}$ is an increasing function of Z, starting at zero for $Z = 0$ and asymptotically reaching one as $Z \to \infty$. As a result, if we can prove that the other function is a decreasing function of Z, for a given Y, then the system is guaranteed to have a unique positive solution (see examples in Figure S8B when this is the case). In STAR Methods "Z_1 positively regulates X_C in the presence of P and D terms" we show that X_C is an increasing function of Z_1 for the antithetic controller, given Y. And since the steady-state X_1 equations for the two integral controllers have the same form (compare Equations S38 and S45), it follows that X_C is an increasing function of Z given Y for the integral controller presented in Section "Constructing a PID controller with a different integral controller architecture". Thus, $\frac{\beta_Z}{\gamma_Z} \frac{\mu Y}{\mu Y + \theta X_C(X_1(Z,Y))}$ is a decreasing function of Z given Y. This demonstrates the existence of a unique steady state solution for the PID controller developed from the integral controller presented in Section "Constructing a PID controller with a different integral controller architecture". However, we are not guaranteeing that is stable, which depends on the gain in the process. When unstable, it can result in limit cycles as we show in Figure 7 for the *I* only case.

The proof above applies for any value of β_Z/γ_Z. However, we now put forward the requirement that $\beta_Z/\gamma_Z>1$, and argue that this is a design choice for the integral controller to function appropriately (I only case where $X_C(X_1(0,Y)) = 0$). This can also be gleaned from Figure S8B (I only case), where it can be seen that it is only when $\beta_Z/\gamma_Z>1$ and $Z \gg K_Z$ that a steady-state solution can occur where $\frac{Z}{Z+K_Z} \approx 1$. This is a condition to achieve the integral action. Figure S8B shows that for $\beta_Z/\gamma_Z<1$, the solution has to occur at $\frac{Z}{Z+K_Z} < \beta_Z/\gamma_Z<1$. Thus, for this case, approximate integral control will become more degraded the smaller that β_Z/γ_Z becomes. As designers, we are in control of enforcing $\beta_Z/\gamma_Z>1$ and $Z \gg K_Z$ for the operation regimes of interest. A more stringent requirement of $\frac{\beta_Z}{\gamma_Z} \frac{\mu Y}{\mu Y + \theta X_C(X_1(0,Y))} > 1$ is required for a functional integral controller if P and/or D control is present, where $X_C(X_1(0,Y))>0$.

DATA AND CODE AVAILABILITY

The code used for all simulations is available at https://github.com/mgschiavon/bioPIDcontrol.